

INFORMATION TO USERS

This was produced from a copy of a document sent to us for microfilming. While the most advanced technological means to photograph and reproduce this document have been used, the quality is heavily dependent upon the quality of the material submitted.

The following explanation of techniques is provided to help you understand markings or notations which may appear on this reproduction.

1. The sign or "target" for pages apparently lacking from the document photographed is "Missing Page(s)". If it was possible to obtain the missing page(s) or section, they are spliced into the film along with adjacent pages. This may have necessitated cutting through an image and duplicating adjacent pages to assure you of complete continuity.
2. When an image on the film is obliterated with a round black mark it is an indication that the film inspector noticed either blurred copy because of movement during exposure, or duplicate copy. Unless we meant to delete copyrighted materials that should not have been filmed, you will find a good image of the page in the adjacent frame. If copyrighted materials were deleted you will find a target note listing the pages in the adjacent frame.
3. When a map, drawing or chart, etc., is part of the material being photographed the photographer has followed a definite method in "sectioning" the material. It is customary to begin filming at the upper left hand corner of a large sheet and to continue from left to right in equal sections with small overlaps. If necessary, sectioning is continued again—beginning below the first row and continuing on until complete.
4. For any illustrations that cannot be reproduced satisfactorily by xerography, photographic prints can be purchased at additional cost and tipped into your xerographic copy. Requests can be made to our Dissertations Customer Services Department.
5. Some pages in any document may have indistinct print. In all cases we have filmed the best available copy.

University
Microfilms
International

300 N. ZEEB RD., ANN ARBOR, MI 48106

8209092

Aksaci, Denginur

**EVALUATION OF A FLUORAPATITE-SPINEL CERAMIC AS A BONE
IMPLANT**

Iowa State University

PH.D. 1981

**University
Microfilms
International** 300 N. Zeeb Road, Ann Arbor, MI 48106

PLEASE NOTE:

In all cases this material has been filmed in the best possible way from the available copy. Problems encountered with this document have been identified here with a check mark .

1. Glossy photographs or pages
2. Colored illustrations, paper or print
3. Photographs with dark background
4. Illustrations are poor copy _____
5. Pages with black marks, not original copy _____
6. Print shows through as there is text on both sides of page _____
7. Indistinct, broken or small print on several pages
8. Print exceeds margin requirements _____
9. Tightly bound copy with print lost in spine _____
10. Computer printout pages with indistinct print _____
11. Page(s) _____ lacking when material received, and not available from school or author.
12. Page(s) _____ seem to be missing in numbering only as text follows.
13. Two pages numbered _____. Text follows.
14. Curling and wrinkled pages _____
15. Other _____

**University
Microfilms
International**

**Evaluation of a fluorapatite-spinel ceramic
as a bone implant**

by

Denginur Aksaci

**A Dissertation Submitted to the
Graduate Faculty in Partial Fulfillment of the
Requirements for the Degree of
DOCTOR OF PHILOSOPHY**

**Department: Materials Science and Engineering
Major: Metallurgy**

Approved:

Signature was redacted for privacy.

In Charge of Major Work

Signature was redacted for privacy.

For the Major Department

Signature was redacted for privacy.

For the Graduate College

**Iowa State University
Ames, Iowa**

1981

TABLE OF CONTENTS

	Page
ABSTRACT	v
INTRODUCTION	1
LITERATURE REVIEW	4
Ceramics as Hard Tissue Implants	4
Aluminum oxide	4
Bioglass	6
Calcium phosphate salts	7
Fluorapatite and spinel	14
Fracture Mechanics	23
Brittle fracture and crack propagation	23
Theoretical strength	23
Griffith-Orowan-Irwin analysis	26
Statistical nature of strength	30
Strength and fracture surface work	32
Static fatigue	36
Effects of microstructure	40
Bend test	42
EXPERIMENTAL PROCEDURE	48
Selection of the Composition	48
Specimen Preparation	52
Specimen preparation for x-ray diffraction	52

	Page
Specimen preparation for optical microscopy, bend test and solubility test	52
X-Ray Diffractometer Studies	53
Optical Microscope Studies on Fluorapatite-Spinel Specimens	54
Study of the Bending Strength	55
Scanning Electron Microscope Studies	58
Solubility Studies	58
Soft Tissue Reaction Test	59
Implants	59
Microscopic Analysis of the Recovered Implant	66
RESULTS AND DISCUSSION	68a
X-Ray Diffraction	68a
Optical Microscopy	68a
Bending Strength	68a
Scanning Electron Microscope Studies	80b
Solubility Studies	93
Soft Tissue Reaction Test	99
Implants In-Vivo	102
Microscopic Analysis of the Implant- Tissue Sections	107
CONCLUSION	122
BIBLIOGRAPHY	123

	Page
ACKNOWLEDGMENTS	128
APPENDIX A	129
Ringer's Solution	129
APPENDIX B	130
Confidence Intervals for Means and the Student's t Test	130
APPENDIX C	132
Comparison of Means by the Student's t Test	132

ABSTRACT

The objective of this study was to produce a ceramic that can be used as a hard tissue implant. After investigation of several mixtures of tricalcium phosphate, calcium fluoride, magnesium carbonate and alumina, a composite of fluorapatite and spinel was selected as the ceramic material. The ability to prepare sound samples and the minimum solubility in tissue fluids were the main reasons for the selection of a composite with one mole of fluorapatite to three moles of magnesium aluminate spinel.

The ceramic was tested to determine the effect of porosity on strength so that the optimum combination of microstructure and mechanical properties could be obtained. The effect of the duration of stay in the physiological environment on the bending strength was determined after in vitro tests in Ringer's solution for porous and non-porous bars, and also after in vivo tests of non-porous subcutaneous implants.

Porous bone bridges implanted in dogs were studied in terms of bone ingrowth, implant stabilization and tissue compatibility. Thin sections of the bone-ceramic interface were prepared and analyzed using optical microscopy with polarized transmitted light.

The results of the tests in vivo and in vitro showed that the fluorapatite-spinel ceramic can be successfully used as a permanent hard tissue implant.

INTRODUCTION

Defects in bone, as a result of disease, trauma or congenital reasons, are a frequent occurrence. These are usually filled with bone graft which is, in most cases, autogenous bone, and sometimes homograft or heterograft bone. However, there are problems with all types of grafts. Homograft bone, while quite functional, is not always readily available. Autogenous bone is usually taken from the iliac crest, which involves another incision. Heterograft bone has been tried without conspicuous success. Therefore, a need for a synthetic material is obvious.

The success of a biomaterial or implant is highly dependent on three major factors: the properties of the implant, the condition of the recipient, and the competency of the surgeon who implants and monitors progress of the implant. The properties required from an implant are:

1. Acceptance of the implant by the tissue
2. Non-toxic and non-carcinogenic
3. Chemically inert and stable (no time dependent degradation)
4. Adequate mechanical strength
5. Adequate fatigue life
6. Sound engineering design
7. Proper weight and density

8. Relatively inexpensive, reproducible, and easy to fabricate and process on a large scale.

Generally, two classes of materials have been used to replace hard tissue: metals (1) and polymers (2). The metals are usually Vitallium and type 316, 316L and 317 stainless steel, although the precious metals, tantalum and titanium are also sometimes used. Advantages of metal implants are high-impact tensile strength, high resistance to wear, and ductile absorption of high strain energy. However, metals have some disadvantages like low biocompatibility, corrosion in physiological environment, mismatch of mechanical properties with tissues and too high density. The polymers used for tissue replacement are usually polyethylene and polymethylmethacrylate cement. Although polymers are easy to fabricate and have low densities, their time-dependent degradation and low mechanical strengths are their major disadvantages. Both metals and polymers are walled off by the body with its foreign body response mechanism. This produces a fibrous capsule which may permit motion under stress. Excess movement causes inflammation, hard tissue resorption, and failure. This need for other materials has led investigators to study ceramic materials in addition to metals and polymers.

Some ceramic biomaterials are considered to be inert,

non-toxic, non-inflammatory and superior in adhesion to surrounding tissue when compared with metals and polymers (3). Research on ceramic hard tissue implants has been concentrated primarily on aluminum oxide, soda-lime-silica glass and calcium phosphate compounds. These materials will be discussed in more detail in the literature review, as well as the fracture mechanics and strength testing of ceramics, mainly the flexure or bend test.

The fluorapatite-spinel composite, selected to be investigated as a hard tissue implant in this study, will be evaluated in terms of the effects of porosity and physiological environment on bend strength. Two tests in vivo were conducted to determine if the bone would grow into the ceramic, and if the implant would be well-tolerated by the surrounding tissues. The results of these tests will also be discussed.

LITERATURE REVIEW

Ceramics as Hard Tissue Implants

The use of plaster of Paris to fill bony defects was a historical precursor to much of the present work(4). Unfortunately, due to the large surface area of these minute hydrated calcium sulphate crystals, plaster of Paris resorbs too quickly to be effective. After World War II, Helmut Bruckmann developed a silicate ceramic, which was impregnated with epoxy resins to make it non-porous and to produce the mechanical properties of bone (5). This product, called Cerosium, was the first composite of ceramic and polymer. Cerosium has now been abandoned because long term tests proved the organic polymer to be carcinogenic. Later, research on ceramic materials was concentrated primarily on aluminum oxide, soda-lime-silica glass and calcium phosphate salts.

Aluminum oxide

Aluminum oxide is a strong, pure, dense ceramic material for which the technology of production is highly developed. It causes minimal foreign body response, and is a good electrical and thermal insulator. The foreign body response of metals may be related to their electrical conductivity because they provide a path for electric currents generated by electrochemical or piezoelectric

potentials. Because of its high strength and insolubility, aluminum oxide is one of the best chemically inactive ceramic compositions (6, 7). Research is being conducted in Europe using dense aluminum oxide to replace the metal femoral component of total hip joint replacements (8). Also, the dense aluminum oxide ball shows promise of reduced wear of the dense polyethylene acetabulum, and of improved synovial lubrication (9). The frictional characteristics and inertness of alumina are related to its crystal structure (10). The array of oxygen atoms makes the material hydrophilic and a surface layer of water on ultra smooth surface finish is said to account for the low coefficient of friction measured in laboratory tests. Porous alumina with pore size 100-750 microns was used for implants placed subperiosteally as alveolar ridge augmentation onlays in monkeys (11). Clinical and radiographic examination during the postoperative period revealed rapid healing and anchorage of the implant in the animals. Tooth root replica implants, made from alumina ceramic material of solid structure coated with a porous layer, were used as dental implants in monkeys (12). Fibrous and mineralized tissue ingrowth of the porous layer of the implants was found. The implants became firmly anchored to the host and no epithelial downgrowth along the ceramic was found.

Bioglass

Soda-lime-silica glass has been extensively tested by Hench, who considers it a promising material for bonding to bone (13). This material, named bioglass, has enough P_2O_5 added to make the $CaO:P_2O_5$ ratio similar to hydroxyapatite, the main constituent of the mineral part of bone. The bonding ability of bioglass to living bone is dependent on controlled surface reactions. Three types of reactions occur in a simulated physiological solution depending on bioglass composition (14):

1. A calcium phosphate film and SiO_2 -rich layer form simultaneously for bioglasses which have low silica content (less than 46 mol% SiO_2).
2. A SiO_2 -rich layer forms first and a calcium phosphate film develops later between the aqueous environment and the SiO_2 -rich layer for bioglasses whose SiO_2 content is between 46-55%.
3. A calcium phosphate film does not form for glasses whose SiO_2 content is more than 60 mol%.

The glasses of group (1) and (2) have the ability to bond to living bone within 30 days and the glasses of group (3) do not have this ability. Therefore, the formation of a calcium phosphate film on the glass surface in a simulated physiological solution is indicative of the ability to

bond to living bone.

Calcium phosphate salts

Since it was discovered that hard tissues, bones and teeth, were characterized by an inorganic phase in which calcium phosphate plays a dominant role, medical researchers have considered this salt as a means to influence healing processes of bony tissues.

Already in the early years of this century, Albee suggested and tested (in animals and patients) the possible application of tricalcium phosphate in fracture healing (15). However, since these salts were only available in powder form, applications were limited to slurries, which served no practical purpose. The fact that these slurries were well tolerated and replaced eventually by new bone, kept interest in calcium phosphate salts, especially those with a Ca/P ratio close to that of bone (1.5 - 1.7). Attention was focused on calcium phosphate salts in the form of solid blocks that had sufficient strength to be machined to the right shape, to be handled by the surgeon, and to withstand physiological loads (16-27).

Bone is composed of 40% organic material (of which 90-96% is collagen) and the rest is mineral (28). The major subphase of the mineral consists of submicroscopic crystals of an apatite of calcium and phosphate resembling

hydroxyapatite crystal structure. There are other ions, such as citrate ($C_6H_5O_7^{4-}$), carbonate (CO_3^{2-}), fluoride (F^-), and hydroxyl ions (OH^-), which may give some other subtle differences in the microstructural features of bone. The apatite crystals are formed as slender needles 200-400 Å long by 15-30 Å thick in the collagen fiber matrix. These mineral containing fibrils are arranged into lamellar sheets (3-7 μm thick). The sheets run helically with respect to the long axis of cylindrical osteon (sometimes called the Haversian system), as shown in Fig. 1 (28).

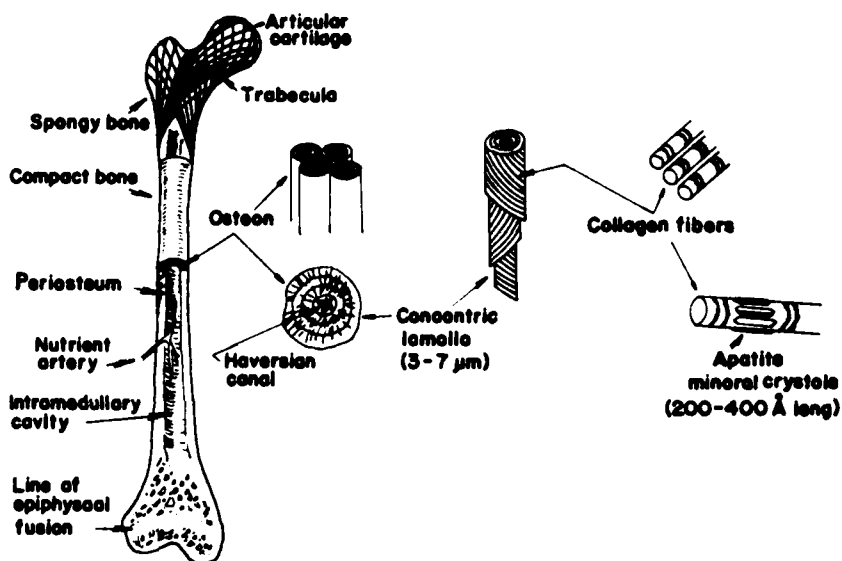


Figure 1. Micro- and macrostructure of a bone

The osteon is made up of from 4 to 20 lamellae arranged in concentric rings around the Haversian canal. Between these osteons the interstitial systems are dispersed and the limits of the Haversian and interstitial systems are sharply divided by the cementing line. The metabolic substances can be transported by the intercommunicating systems of canaliculi, lacunae, and Volkman's canal, which are connected with the marrow cavity. The external and internal surfaces of the bone are called periosteum and endosteum, respectively, and both have osteogenic properties.

Long bones, such as the femur, are usually made of spongy and compact bone. The spongy bone consists of three-dimensional branching of bony or trabeculae interdispersed by bone marrow. The spongy bone changes gradually into compact bone toward the midlength of the bone.

Teeth are also made of mineralized tissues. All teeth have two portions: the crown and the root, demarcated by the gingiva (gum). The root is placed in a socket, called the alveolus, in the maxillary (upper) or mandibular (lower) bone. A sagittal cross section of a permanent tooth is shown in Fig. 2 (29) to illustrate various structural features.

Tooth enamel is the hardest substance found in the body and consists almost entirely of calcium phosphate

salts (97%) in the form of large apatite crystals (28). Dentin is another mineralized tissue whose distribution of organic matrix and mineral is similar to regular bone in composition and physical properties. Dentinal tubules ($3-5\mu\text{m}$ diameter) radiate from the pulp cavity toward the periphery and penetrate every part of dentin. Collagen fibrils ($2-4\mu\text{m}$ diameter) are filled inside the dentinal tubules in the longitudinal direction, and the interface is cemented by protein-polysaccharides.

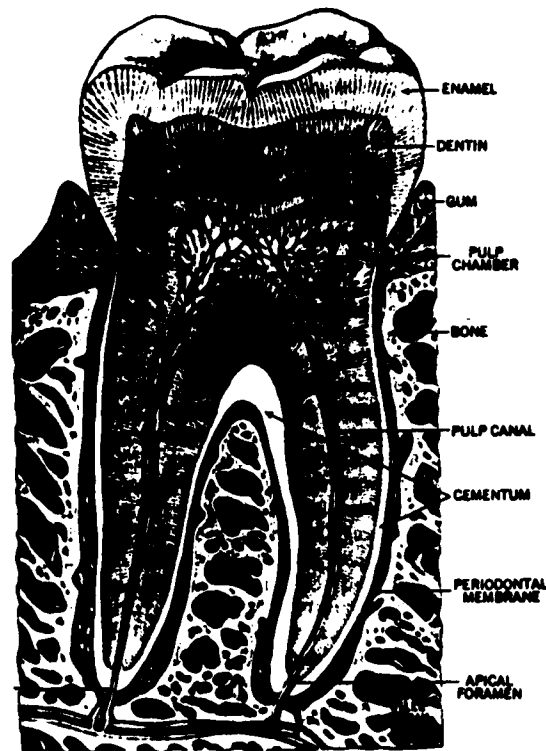
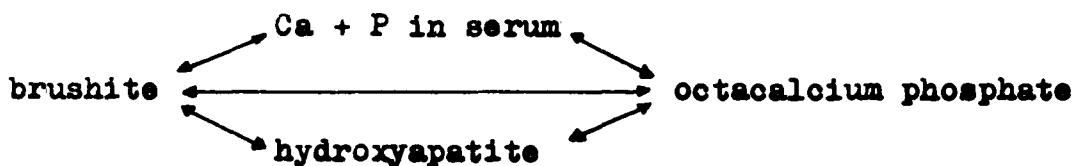


Figure 2. Cross section of a human molar.

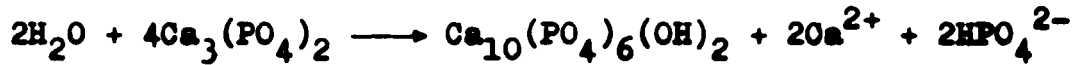
Cementum covers most of the root of the tooth with coarsely fibrillated bone substance but is devoid of canaliculi, Haversian systems, and blood vessels. The pulp occupies the cavity and contains thin collagenous fibers running in all directions and not aggregated into bundles. The ground substances, nerve cells, blood vessels, etc., are also contained in the pulp. The periodontal membrane anchors the root firmly into the alveolar bone and it is made mostly of collagenous fibers plus glycoproteins (protein-polysaccharides complex).

Although it is generally assumed that hydroxyapatite, $\text{Ca}_{10}(\text{PO}_4)_6(\text{OH})_2$, is the main constituent of bone mineral, other salts as brushite, $\text{CaHPO}_4 \cdot 2\text{H}_2\text{O}$, and octacalcium phosphate, $\text{Ca}_8\text{H}_2(\text{PO}_4)_6 \cdot 5\text{H}_2\text{O}$, also play an important role. According to de Groot (15), an equilibrium exists, which can be simply written as:

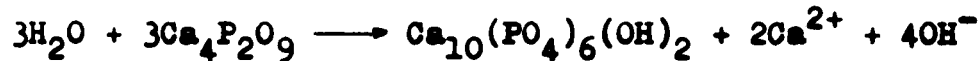


A variety of other well-known calcium phosphate salts cannot exist in physiological conditions, among which tricalcium phosphate, or whitlockite, is the most well-known. Whitlockite, $\text{Ca}_3(\text{PO}_4)_2$, is unstable in water

according to the reaction:



Thus, a powder with $\text{Ca/P} = 3/2$, and in equilibrium with water, should not be considered as a whitlockite, but as an apatite with lattice defects. Another example is calcium tetrphosphate:



Therefore, due to the mutual dynamical equilibria as described by de Groot, and the instabilities of other salts in physiological solution, surfaces of particles with Ca/P ratios varying from 1 (brushite) to 2 (tetra-calcium phosphate) will be the same after incubating in physiological fluid.

Studies of Peelen et al. showed that an important property is the porosity (21). Peelen distinguished microporosity (pores with the size of powder particles, that are left when the particles are not completely fused during the sinter-process) and macroporosity (pores of several hundred microns). Microporosity determines degradation rates in conjunction with other factors such as species, animal age and implant site. Macropores

allow bony ingrowth. Degradation takes place in two steps: physicochemical interaction with body liquids releases individual particles, which in turn are digested intracellularly by phagocytosing cells. Depending on microporosity, the release of isolated particles, and hence the rate of degradation, may occur fast or slow. Thus, rapidly degradable and slowly degradable calcium phosphate ceramics can be prepared.

The nature of bone growth into porous ceramics has been studied by several researchers (30, 31). The pores must be big enough to allow the development of the organic and inorganic components of bone as well as the bone cells. There must be enough room for blood vessels, because they carry the calcium and phosphorus necessary for mineralization and nourishment of the ingrown tissue. The pores must also interconnect to allow the blood vessels to anastomose freely with one another. Pores greater than 100 μm in size were found to be necessary for ingrowth of mineralized bone. β -tricalcium phosphate implants containing interconnecting pores ranging from 100 to 300 μm in size were tested as bone bridges in dogs to study the process of bone replacement of the prostheses (31). The replacement began with an ingrowth of cellular loose connective tissue, which was replaced later by dense connective tissue. Around the periphery of this

dense fibrous connective tissue, osteoid tissue became evident and on later specimens, this mixture was converted to bone - which at first was in the form of spicules but later took on the characteristics of lamellar bone with tricalcium phosphate particles seen within its lacunae. The progressive replacement occurred in a circumferential pattern, but most heavily at the bone-prosthesis interface. Another study on the regeneration of bone in coral-line (coral-like) hydroxyapatite implants in the mandibles of dogs revealed that 11, 46, and 88% of the implant areas were filled with regenerated bone at two, four and six months, respectively (30). The regenerated bone was a woven type at two months, but changed to a lamellar type by six months. In two implanted defects examined at 12 months, biodegradation of 29 percent of the implant had occurred, but biodegradation began after the bone had regenerated.

Fluorapatite and spinel

Calcium phosphate compounds are difficult to fire to produce a dense ceramic. By mixing them with another solid, two advantages result:

1. The problem of forming and firing is minimized,
2. The chemistry can be more effectively controlled if the second phase is itself extremely insoluble.

In this study, fluorapatite, $\text{Ca}_{10}(\text{PO}_4)_6\text{F}_2$, was used to form a composite ceramic with MgAl_2O_4 spinel.

Calcium apatites generally tend to undergo transformation reactions in neutral or weakly acidic solutions to yield acidic orthophosphates (32). Fluoride containing apatites are usually more acid stable than hydroxyapatite or whitlockite, but when decomposed in acid, frequently yield calcium fluoride. Also, carboxylate ions, especially under acidic conditions, accelerate the decomposition by the formation of complexes with calcium ions, thus resulting in decalcification of the apatite. Although apatites can resist decalcification-induced decomposition by the formation of calcium-deficient apatites, the properties of these are not well-documented.

Sintered apatites, both hydroxyapatites and fluorapatites, were stored in solutions of citric, acetic, or lactic acid, of concentrations up to 10% w/w, buffered to pH 4, 5 or 6 with the sodium salt for periods of up to 6 months, after which the mechanical properties of the compacts were measured. In no case was there a decrease in the mechanical properties of more than 10 percent (32).

Solubility of fluorapatite in several solutions are given in Table 1 (33). Subcutaneous implants of fluorapatite in the form of dense rods in rats showed no adverse tissue response and no detectable attack on the

apatite surface (34).

Table 1. Solubility of fluorapatite (mg/l) at 34 C

Solution	pH							
	7.5	7.0	6.5	6.0	5.5	5.0	4.5	4.0
Water	1.8	3.0	5.4	11.6	21.3	47.3	108	253
0.05M KCl	3.4	5.2	9.0	15.5	32.8	70.3	153	339
0.15M KCl	4.5	6.9	11.2	19.7	41.1	87.9	190	417
0.05M KCl								
+5 mM F	1.5	2.5	4.6	8.8	19.5	45.9	109	263
+5 mM Ca	0.007	0.02	0.07	0.23	1.2	6.7	34.9	157
+5 mM P	0.31	0.55	1.1	2.3	6.8	21.2	65.2	196
+0.1M P	1.4	1.7	2.0	2.1	3.8	8.2	24.3	78.3
Unstimulated saliva					<1 µg			
Stimulated saliva	<1 µg							

Also, the problem of forming and firing is minimized when CaF_2 is added into $\text{Ca}_3(\text{PO}_4)_2$ to form fluorapatite upon firing. $\text{Ca}_3(\text{PO}_4)_2$ is subject to a crystallographic inversion, which causes internal fractures leading to low strength in pure whitlockite specimens, when cooled from above 1100 C in the firing process, Fig. 3 (35).

Selection of a second phase to be mixed with fluorapatite imposes chemical, physical and processing constraints. Since some solubility is inevitable, such a material must be chosen that, it will be compatible with body tissues in small quantities. Both Mg^{2+} and Al^{3+} are ions of such character. Therefore, MgAl_2O_4 spinel

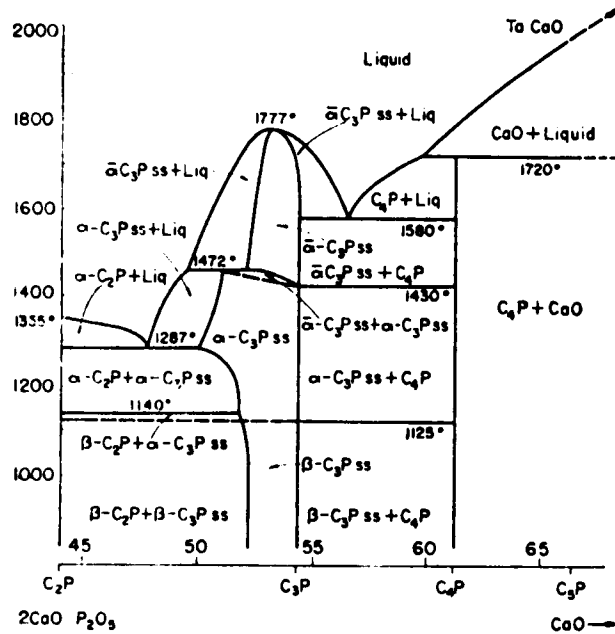


Figure 3. System $\text{CaO}-2\text{CaO}\cdot\text{P}_2\text{O}_5$.
 $\text{C} = \text{CaO}$, $\text{P} = \text{P}_2\text{O}_5$

is a suitable material for this purpose. The solubility of spinel in aqueous solutions is extremely low. Products of hydration are not harmful, $\text{Mg}(\text{OH})_2$ and $\text{Al}(\text{OH})_3$ both being mild and tolerated by body tissues. It is insoluble in HNO_3 , very slightly soluble in dilute HCl , and slightly soluble in H_2SO_4 (36). It does not form intermediate compounds when a mixture of fluorapatite and spinel are fired together. It has a melting behavior compatible with

ceramic firing processes (m. p. of $\text{MgAl}_2\text{O}_4 = 2135 \text{ C}$ (36), m. p. of $\text{Ca}_{10}(\text{PO}_4)_6\text{F}_2 = 1647 \text{ C}$ (37). Tooth roots with regions of controlled porosity for tissue ingrowth were made from an equimolar mixture of $\text{Ca}_3(\text{PO}_4)_2$ and MgAl_2O_4 at Iowa State University, and were implanted sub-mucosally in the mandible and maxilla of dogs. It was observed that the tissue response was acceptable and strong attachment had occurred (25). Disk-shaped implants (approximately 1 cm in diameter and 1 mm thick) of spinel were implanted in the paraspinalis muscle of New Zealand rabbits up to four months, and no surface degradation of the ceramic was detected using scanning electron microscopy (38). The biocompatibility compared favorably with the clinically used cast Co-Cr-Mo alloy implants and the UHMWPE (ultra high molecular weight polyethylene) implants. Spinel samples with 48-54% open porosity have been tested as dental anchors in Miniature Swine and they showed excellent hard tissue biocompatibility and no inflammatory response (39).

Ceramic considerations also favor the fluorapatite-spinel composite. Normal spinel is a cubic close packed assembly of oxygen ions with Mg^{2+} tetrahedrally coordinated with oxygen, and Al^{3+} octahedrally coordinated with oxygen. The unit cell contains 32 oxygen ions. There are 64

interstitial spaces which have tetrahedral coordination with oxygen and 32 interstitial spaces which have octahedral coordination with oxygen. Since eight magnesium ions and sixteen aluminum ions occupy these sites, only one-eighth of the tetrahedral sites and one-half of the octahedral sites are occupied. This structure lends itself to liberal substitution and some distortion. Despite the wide range of solid solutions for normal and inverse spinels, the structure is ideal for compounding with calcium phosphates as a composite. Neither Ca^{2+} nor P^{5+} ions can enter into solid solution with MgAl_2O_4 spinel because of ionic size difference between Ca^{2+} and Mg^{2+} , and charge difference between P^{5+} and Al^{3+} .

The lattice constant of spinel is given as 8.0800 Å (40). Fluorapatite has hexagonal close packed structure with 42 atoms per unit cell. Its lattice constants are: $a = 9.3684$ Å, and $c = 6.8841$ Å (41).

Bulk, shear and Young's moduli (K, G and E, respectively) for fluorapatite, hydroxyapatite and MgAl_2O_4 spinel are given in Table 2. Young's moduli for cortical bone, osteoid tissue, fibrous tissue, human dentin and human enamel are given in Table 3, as well as the moduli for two biomaterials, steel and high density polyethylene (HDPE), in completely dense state, 50% porous state and 50% porous state with uniform bone ingrowth. Bend strengths

(moduli of rupture) for spinel and human cortical bone are given in Table 4.

Table 2. Bulk, shear and Young's moduli for mineral fluorapatite and hydroxyapatite, synthetic hydroxyapatite, and spinel (moduli in 10^6 psi)

Sample	K	G	E	Reference
FAp (mineral) ^a	13.63	6.73	17.40	(42)
OHAp (mineral) ^a	12.91	6.45	16.53	(42)
OHAp (synth.) ^a	12.76	6.60	16.97	(42)
Spinel ^b			34.50	(43)
Spinel ^c			35	(44)
Spinel ^d	31.5	14.8	38	(44)
Spinel ^e		13	34	(44)
Spinel ^f		16.0	42	(44)

^aIdeally dense material.

^bSintered; ca. 5% porosity.

^cHot pressed; 99% dense; four-point bend test.

^dHot pressed; 98% dense; dynamic method.

^eSlip cast and sintered rod specimens; at least 95% dense; torsional loading.

^fExtrapolated value for theoretical density.

Table 3. Young's moduli for hard tissues and some biomaterials (in 10^6 psi)

Material	E	Reference
Cortical bone	2	(45)
Osteoid tissue	0.030	(45)
Fibrous tissue	0.015	(45)
Human dentin	2.67	(46)
Human enamel (cusp)	12.3	(46)
Human enamel (side)	11.3	(46)
Steel	28	(45)
Porous steel ^a	7	(45)
Bone/steel ^b	9.4	(45)
HDPE	0.1	(45)
Porous HDPE ^a	0.025	(45)
Bone/HDPE ^b	0.62	(45)
Osteoid/HDPE ^b	0.056	(45)
Fibrous/HDPE ^b	0.042	(45)

^aContains approximately 50% porosity.

^bThe moduli were estimated by assuming 50% porosity and uniform bone ingrowth (45).

Table 4. Bend strengths (MOR) for spinel and human cortical bone (in psi)

Material	MOR	Reference
Spinel ^a	13,000	(43)
Spinel ^b	32,000	(44)
Spinel ^c	19,000	(44)
Spinel ^d	12,000	(44)
Humerus	27,729	(47)
Radius	31,426	(47)
Ulna	31,426	(47)
Femur	25,169 ± 1,564	(47)
Tibia	29,720	(47)
Fibula	31,426	(47)

^aSintered; ca. 5% porosity.

^bHot pressed; 99% dense; value from four-point bend test.

^cSintered; 95% dense.

^dSlip cast and sintered; at least 95% dense.

Fracture Mechanics

Ceramic materials almost always fail by brittle fracture. In order to improve their mechanical properties, it is necessary to understand the mechanisms controlling brittle fracture.

Brittle fracture and crack propagation

Brittle fracture requires two conditions: (1) production of a crack, (2) propagation of the crack to final fracture. Either of these conditions can control the overall fracture process.

The criterion for plastic deformation is that $\tau_{\max} \leq (\sigma_1 - \sigma_3)/2 = \sigma_0/2$. In the same way, the maximum tensile stress is the criterion for fracture (43). In many crystalline materials, fracture occurs along crystallographic planes of high atomic density, which are called cleavage planes. However, fracture follows a random path in glasses and in some crystals.

Theoretical strength The theoretical cohesive strength of a material gives a meaningful measure of the stresses that must be overcome during fracture. It gives the maximum strength to be expected from a given material.

Fracture is the process of separating a solid into two parts. During the separation process, attractive forces act across the incipient fracture surfaces, first increasing, then decreasing with distance of separation, as shown in Fig. 4 (43). Part of this curve can be defined by a relation of the form

$$\sigma = \sigma_{th} \sin \left(\frac{2\pi x}{\lambda} \right) \quad \text{Eq. 1}$$

where σ_{th} is the theoretical strength.

The work per unit area to separate the two planes of atoms can then be calculated as:

$$\int_0^{\lambda/2} \sigma_{th} \sin \left(\frac{2\pi x}{\lambda} \right) dx = \frac{\lambda \sigma_{th}}{\pi} \quad \text{Eq. 2}$$

This work is equated with the surface energy 2γ of the two new surfaces, giving

$$\sigma_{th} = \frac{2\pi\gamma}{\lambda} \quad \text{Eq. 3}$$

Hooke's law may be used near the equilibrium spacing, a_0 ,

$$\sigma = E \frac{x}{a_0} \quad \text{Eq. 4}$$

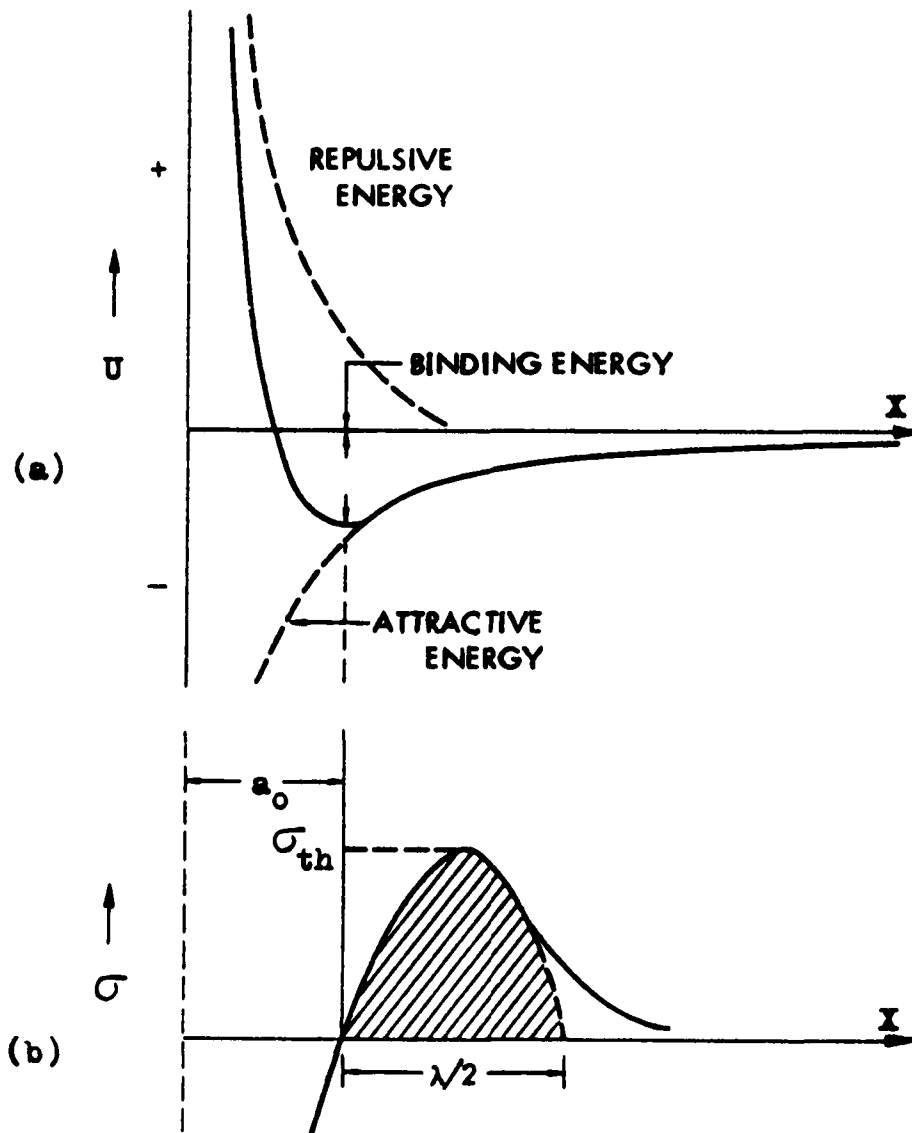


Figure 4. Schematic representation of (a) variation of potential energy with interatomic distance, and (b) force necessary to separate adjacent planes in a crystal

where E is the Young's modulus. For this part of the curve, one obtains from Eq. 1, for small values of X

$$\frac{d\sigma}{dX} = \frac{2\pi\sigma_{th}}{\lambda} \cos\left(\frac{2\pi X}{\lambda}\right) \approx \frac{2\pi\sigma_{th}}{\lambda} \quad \text{Eq. 5}$$

Equating this with $d\sigma/dX$ from Eq. 4,

$$\frac{2\pi\sigma_{th}}{\lambda} = \frac{E}{a_0} \quad \text{Eq. 6}$$

Substituting Eq. 6 in Eq. 3,

$$\sigma_{th} = \left(\frac{E\gamma}{a_0}\right)^{1/2} \quad \text{Eq. 7}$$

Assuming λ is similar in magnitude to a_0 , σ_{th} may be obtained from Eq. 6 as

$$\sigma_{th} \approx \frac{E}{5} \text{ to } \frac{E}{10} \quad \text{Eq. 8}$$

Strengths of this order are obtained only in thin fibers of fused silica and whiskers of oxides as Al_2O_3 . Most commercial materials have strengths in the range of $E/100$ to $E/1000$.

Griffith-Crowan-Irwin analysis In order to explain this discrepancy between the theoretical and

actual strengths of materials, Griffith (48) assumed that small cracks in the body of brittle materials were causing their low strength. He assumed that a crack propagates when the decrease in stored elastic energy associated with its extension exceeds the increase in surface energy associated with the formation of new surfaces. For elliptical cracks of major axis $2c$ in a thin plate, this condition is expressed as

$$\frac{d}{dc} \left(\frac{\pi c^2 \sigma^2}{E} \right) = \frac{d}{dc} (4\gamma c) \quad \text{Eq. 9}$$

or

$$\sigma_f = \left(\frac{2E\gamma}{\pi c} \right)^{1/2} \approx \left(\frac{E\gamma}{c} \right)^{1/2} \quad \text{Eq. 10}$$

Another approach considers the stress concentration at the tip of a flaw. Inglis (49) showed that the maximum stress in the vicinity of the crack tip may be expressed as

$$\sigma_m = 2\sigma \left(\frac{c}{\rho} \right)^{1/2} \quad \text{Eq. 11}$$

where ρ is the radius of the crack tip. Failure would occur when the stress at the crack tip exceeds the theoretical strength of the material ($\sigma_m = \sigma_{th}$).

Orowan (50) assumed that the minimum radius of curvature at the crack tip is of the order of a magnitude

of the interatomic spacing, a_0 . If ρ in Eq. 11 is replaced by a_0 , and σ_m is replaced by the value of σ_{th} in Eq. 7, the fracture stress, σ_f , becomes

$$\sigma_f = \left(\frac{E\gamma}{4c} \right)^{1/2} \quad \text{Eq. 12}$$

Equations 10 and 12 yield similar predictions for the fracture strength provided that the radius of curvature at the crack tip is of the order of an interatomic spacing.

Orowan (51) included a term γ_p for the plastic or viscous work required to extend a crack by unit area in partially ductile materials:

$$\sigma_f = \left[\frac{E(\gamma + \gamma_p)}{c} \right]^{1/2} \quad \text{Eq. 13}$$

For materials which are not completely brittle, γ_p is generally much larger than γ .

Irwin (52) suggested a crack-extension force G for the case in which a load P is applied to a plate with a crack of length $2c$:

$$G = \frac{P^2}{2} \frac{d(1/m)}{dc} \quad \text{Eq. 14}$$

where m is the slope of the load-extension plot.

G is also expressed as a strain-energy-release rate, which is the rate of loss of energy from the elastic stress field during crack propagation:

$$G = \frac{\pi \sigma^2}{E} \quad \text{Eq. 15}$$

Measured values of G include the energy of plastic or viscous deformation required to propagate the crack. G increases with crack length until a critical value G_0 is reached, at which the crack becomes unstable and propagates rapidly in a brittle manner. According to Kingery et al. (43), the Griffith relation (Eq. 10) can be written

$$\sigma_f = \left(\frac{EG_0}{\pi c} \right)^{1/2} \quad \text{Eq. 16}$$

Stress-intensity factor, K_I , which is given as

$$K_I = \sigma (Y_0)^{1/2} \quad \text{Eq. 17}$$

is also related to the strain-energy-release rate, G . (Y in Eq. 17 is a parameter which depends on the specimen and crack geometry and equals π for a central crack in a thin infinite plate.) For a plane stress condition, $K_I^2 = G E$, and in general when $G = G_0$, $K_I = K_{I0}$, where

K_{Ic} is called the fracture toughness (43).

K_{Ic} is also used to estimate the size of the plastic zone ahead of the crack tip. The length R of the zone, from Dugdale's analysis (53), is

$$R = \frac{\pi}{8} \left(\frac{K_{Ic}}{\sigma_y} \right)^2 \quad \text{Eq. 18}$$

where σ_y is the yield stress of the material.

Statistical nature of strength The fracture strength of a brittle material is statistical in nature, depending on the probability that a flaw capable of initiating fracture at a specific applied stress is present. The observed strength is related to the volume of the material under stress or the surface area of the material under stress. Attempts to develop a statistical theory for the strength of brittle solids involve an assumption about the number of dangerous flaws related to the specimen volume or surface area. However, this relationship changes from one material to another and probably depends on the fabrication method and on treatment after fabrication.

Weibull (54) assumed that the risk of failure is proportional to a function of the stress and the volume of the body:

$$R = \int_V f(\sigma) dv \quad \text{Eq. 19}$$

He used the form for $f(\sigma)$:

$$f(\sigma) = \left(\frac{\sigma}{\sigma_0} \right)^m \quad \text{Eq. 20}$$

where σ_0 is a characteristic strength depending on the distribution function best fitting the data and m is a constant related to the material homogeneity. The larger the value of m , the more homogeneous the material; therefore, as m approaches zero, $f(\sigma)$ approaches unity which means that the probability of failure is equal for all values of stress. As m approaches infinity, $f(\sigma)$ becomes zero for all values of σ less than σ_0 . The probability of fracture becomes unity only when σ equals σ_0 , the characteristic strength. The average strength value measured is given by

$$\sigma_{R=1/2} = \left(\frac{1}{2} \right)^{1/m} \sigma_0 \quad \text{Eq. 21}$$

The ratio of this value to σ_0 gives an indication of the dispersion of observed strength values.

This statistical theory of fracture predicts that

larger samples should be weaker and that the dispersion in values of fracture stress should increase as the median strength increases.

Strength and fracture surface work

For glasses and many crystalline ceramics, surface flaws are generally responsible for the relatively small practical strengths. In polycrystalline ceramics, the difference in thermal expansion coefficients of the phases present in the material gives rise to boundary stresses and the formation of cracks. Stresses set up during cooling of samples from the firing temperature can also be a source of microcracks. Mechanical abrasion of the surface and chemical attack are common sources for crack development.

Brittle fracture can be observed in normally ductile or semibrittle materials under certain test conditions like low temperature, impact loading or restraints on plastic deformation such as notches. The dislocations generated during plastic deformation can coalesce to produce a microcrack that leads to brittle fracture. Dislocations tend to pile up at slip bands, grain boundaries and surfaces, leading to high local stresses which force the dislocations together to form a crack nucleus. Crack formation is possible at an intersection of slip

bands causing a dislocation pile-up and crack initiation as shown in Fig. 5 (43). The fracture stress for semibrittle materials can be expressed as

$$\sigma_f = \sigma_0 + k_1 d^{-1/2} \quad \text{Eq. 22}$$

where

$$k_1 = \left(\frac{3\pi\gamma E}{1-\nu^2} \right)^{1/2} \quad \text{Eq. 23}$$

It is assumed that the band length is proportional to the grain size d . Equation 22 is a Petch-type relation predicting that the strength should increase with decreasing grain size. When the sizes of the initial flaws are limited by the grains in a brittle material, the strength should vary with the grain size according to the Orowan relation:

$$\sigma_f = k_2 d^{-1/2} \quad \text{Eq. 22a}$$

Anisotropic thermal contraction is also suggested as a mechanism for crack initiation in polycrystalline ceramics by Clarke (55). Fracture is assumed to initiate at grain-boundary pores and propagate along the grain boundaries. When the pores are much smaller than the grain size, spontaneous fracture occurs when

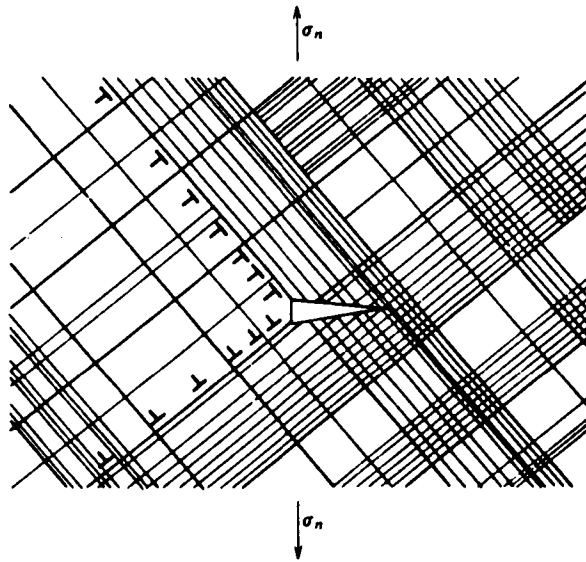


**Figure 5. Dislocation pile-up and crack formation
at intersection of two slip bands (43)**

$$\epsilon = \left(\frac{48 \gamma_b}{E d} \right)^{1/2} \quad \text{Eq. 24}$$

ϵ is the grain-boundary strain and γ_b is the grain-boundary surface energy.

Fracture occurs at the most critical flaw. In engineering practice, care should be taken to minimize the size of the most severe flaw and ensure that it is close to the average flaw size.

In glasses and many ceramic single crystals, the initiation of cracks is the critical stage of rupture process. Once a crack has been initiated, there is no energy-absorbing process like plastic deformation; therefore the crack continues to complete failure. In polycrystalline ceramics, obstacles like grain boundaries can hinder crack propagation. The increase in stress for a crack to change direction at a boundary has been analyzed by Gell and Smith (56), for polycrystalline arrays. The measured fracture surface energies are larger by a factor of 5 to 10 for polycrystals than those determined for single crystals. The large $(\gamma + \gamma_p)$ of the polycrystals associated with the irregular crack paths is responsible for high fracture surface energies.

Kingery et al. (43) suggest that strength of polycrystals depends primarily on single-crystal or grain-boundary fracture surface energies rather than on the

polycrystal ($\gamma + \gamma_p$) values, since single crystals are generally stronger than polycrystals and the strength of polycrystals increases with decreasing grain size.

Static fatigue

In glasses and ceramics, the measured strength depends on the length of time a load is applied. The relationship between the fracture stress (σ_f) and the time to failure (t) can be described by a relation of the form

$$\log t = \frac{A}{\sigma_f} + B \quad \text{Eq. 25}$$

where A and B are constants. This relation cannot be valid at very short times but provides a useful description over the range of data from 0.01 sec to 10,000 sec.

Static fatigue is most pronounced when moisture is present in the atmosphere, and it also shows a temperature dependence.

The fatigue process is associated with two phenomena: (1) a stress corrosion process where the rate of corrosion at the crack tip is increased due to the stress, causing the deepening of the crack which eventually results in failure, and (2) a decrease in the fracture surface work by the adsorption of an active species.

Charles (57) pointed out that the high tensile stress at the crack tip leads to an expansion of the lattice at that point and to a continually increasing stress concentration.

Wiederhorn (58) used the model of stress corrosion to describe the experiments in which the crack velocity of glasses was measured as a function of temperature, environment, and stress-intensity factor. His results are shown in Fig. 6, which indicates three regions in the crack velocity versus stress-intensity factor relation. In region I, the velocity changes exponentially with K_I , as described by the stress-corrosion model. In region II, the crack velocity is nearly independent of K_I but depends on the water-vapor pressure. In region III, the velocity is independent of the environment but it is strongly dependent on K_I .

The stress-corrosion model predicts that the crack velocity varies exponentially with stress-intensity factor:

$$V = V_0 \exp \frac{(-E^* + bK_I)}{RT} \quad \text{Eq. 26}$$

The dependence of crack velocity on stress-intensity factor is also described by the empirical relation

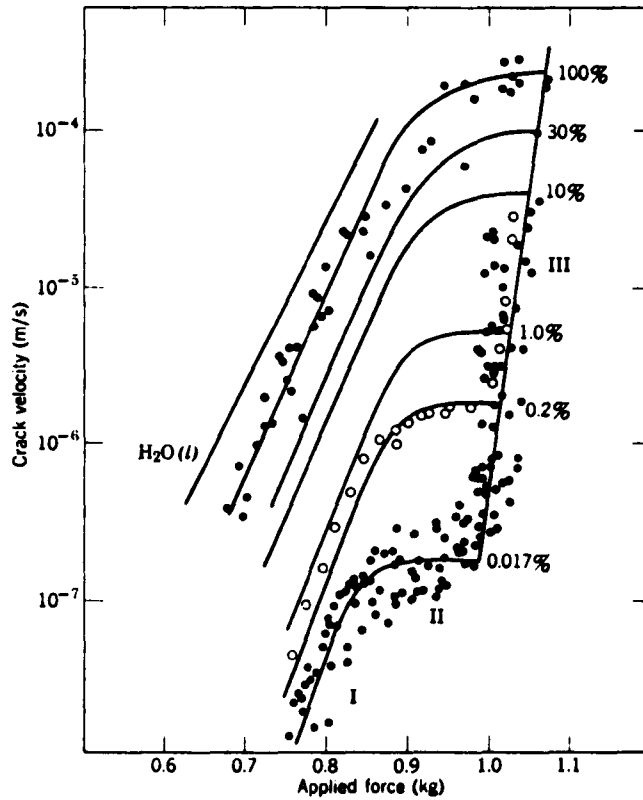


Figure 6. Dependence of crack velocity on applied force for soda-lime-silicate glass. The percentage of relative humidity is given on the right-hand side of the diagram, and the Roman numerals indicate the three regions of crack propagation

$$V = A K_I^n \quad \text{Eq. 27}$$

Typical values of n are in the range of 30 to 40, indicating a strong dependence of crack velocity on stress-intensity.

The work on glasses indicated that under conditions of oscillating stress, the strength behavior could be described by static fatigue, with the relevant time parameter being the sum of the times the specimen spends under the tensile stress.

For a sinusoidal stress as $\sigma(t) = \sigma_0 + \sigma_1 \sin 2\pi\nu t$, the average crack velocity is expressed in terms of the average stress-intensity factor,

$$V_{av} = g A K_{I_{av}}^n \quad \text{Eq. 28}$$

where

$$g = \nu \int_0^{1/\nu} \left[\frac{\sigma(t)}{\sigma_0} \right]^n dt \quad \text{Eq. 29}$$

The average crack velocity then becomes

$$V_{av} = g V_{static} \quad \text{Eq. 30}$$

where V_{static} is obtained from Eq. 27 with K_I taken as $K_{I_{av}}$.

Application of fracture mechanics has introduced the concept of proof testing in ceramic materials. The specimens which survive a proof stress σ_p , corresponding to a stress-intensity factor K_{IP} , must have

$$K_{IP} = \sigma_p (Y_0)^{1/2} < K_{Ic} \quad \text{Eq. 31}$$

Kingery et al. (43) suggest that "knowing the upper limit to the size of cracks which can be present in specimens surviving the proof test and knowing the crack-propagation velocity as a function of stress-intensity factor for the material, one can then in principle guarantee a minimum service life under given stress conditions for all samples".

Effects of microstructure

In most ceramics, the major effect of microstructure on strength is due to the presence of porosity. Pores act as stress concentrators as well as decreasing the cross-sectional area on which the load is applied. Experimental results show that the strength decreases

almost exponentially with increasing porosity.

Ryshkewitch (59) suggested an empirical relation

$$\sigma = \sigma_0 \exp(-nP) \quad \text{Eq. 32}$$

where n is in the range of 4 to 7, and P is the volume fraction porosity. Data for several materials illustrating the effect of porosity are given in Fig. 7.

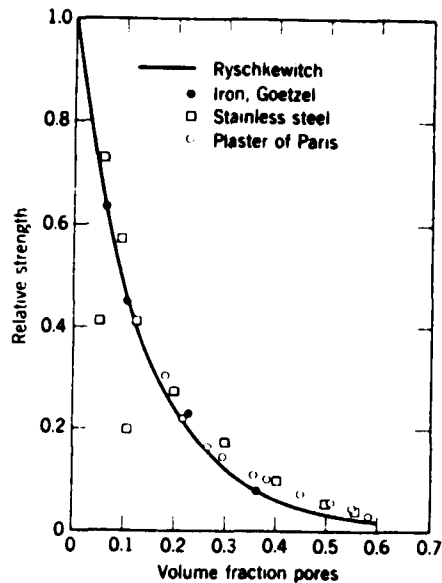


Figure 7. Effect of porosity on the fracture strength (43)

Bend test

Because of the problems associated with direct tension testing of brittle materials, the ceramics industry promoted the well-known bend test as a means for evaluating tensile strengths. This test avoids the need for placing the entire cross section of a specimen in uniform tension, and places only a portion of the cross section in tension. The maximum tensile stresses occur only in the extreme outer fibers on one side of the specimen, with the tensile stresses decreasing to zero at the neutral plane and being balanced by compressive stresses in the specimen on the other side of the neutral plane. Thus, while the test is intended to provide a tensile strength value, it is classified as a bending test because it involves a non-uniform tensile stress field instead of the uniform field in the direct tension test.

As shown in Fig. 8, a bend test specimen is supported close to each end and on the side opposite the supports a uniformly increasing load is applied at a single point centrally located between the supports (three-point loading) or at two points (four-point loading) equidistant from the supports. The load is increased until the specimen fractures.

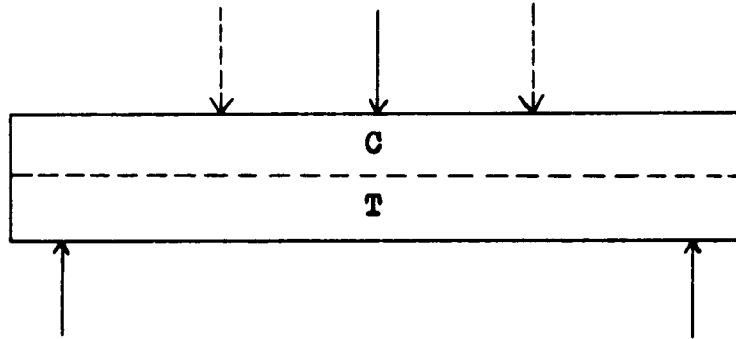


Figure 8. Diagram of a bar flexure specimen. The specimen is supported near the ends and loaded centrally for three-point bending (solid arrow at top) or in four-point bending (dashed arrows at top). The dashed horizontal line is the neutral axis

The maximum stress at fracture is defined as the flexural strength, and is frequently referred to as the modulus of rupture, or MOR. The maximum stress is obtained by using the following equation:

$$\sigma = \frac{M C}{I} \quad \text{Eq. 33}$$

where

σ = extreme fiber stress

M = bending moment

C = distance from the neutral plane of the specimen to the extreme tension fiber

I = moment of inertia of the cross section of the specimen about the neutral axis.

Some assumptions have to be made for the equation to be valid. These are:

1. The material obeys Hooke's law.
2. The stress is distributed linearly across the bent beam and is directly proportional to the distance from the neutral plane.
3. Bending occurs in a plane of symmetry of the beam.
4. The original transverse plane remains a plane after bending occurs and is perpendicular to all longitudinal fibers after bending.
5. There are no shear stresses present in the area where the maximum fiber stress is to be measured.

The specimen for the bend test should be of a size that is large enough to be representative of the material for which it is serving as a sample. To minimize torsional stresses arising from warped specimens or nonplanar test

beds, rockers are generally used on the bottoms of the supports (which are commonly knife edges) and loading is often done through spheres.

Frictional forces should be reduced to a minimum. Since these forces act by grabbing and slipping they produce an extremely erratic effect on the results. These forces are generally reduced by using rounded or rolling knife edges and lubricants with the test specimen. There may be a wedging action due to the concentrated load which could lead to erroneous results in the three-point bend test. With four-point loading, a much larger area of the specimen is under maximum stress, giving a more representative value of the usable strength of the material. As the area under uniform maximum stress increases the strength decreases. This is representative of the size effect.

Shear force and bending moment diagrams for three-point and four-point bend tests are shown in Fig. 9 and Fig. 10, respectively.

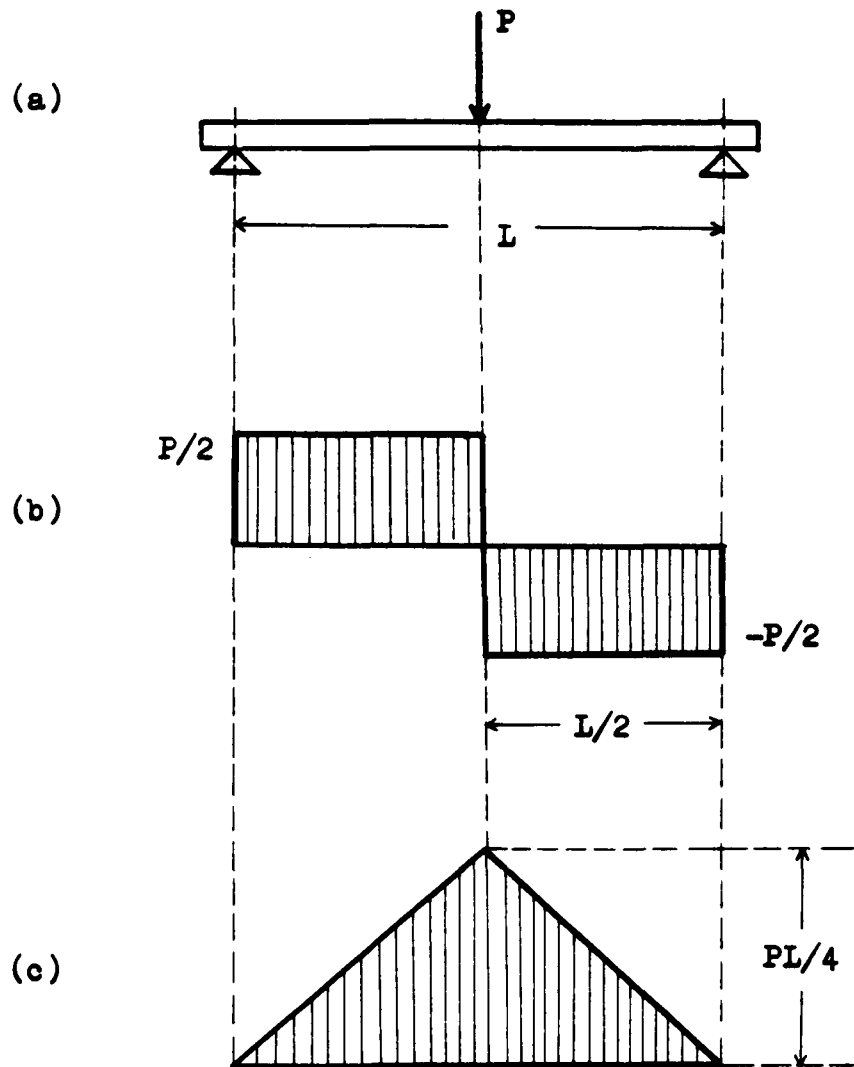


Figure 9. Schematic representation of MOR test:
 (a) Three-point bend test
 (b) Shear diagram for three-point bend test
 (c) Moment diagram for three-point bend test

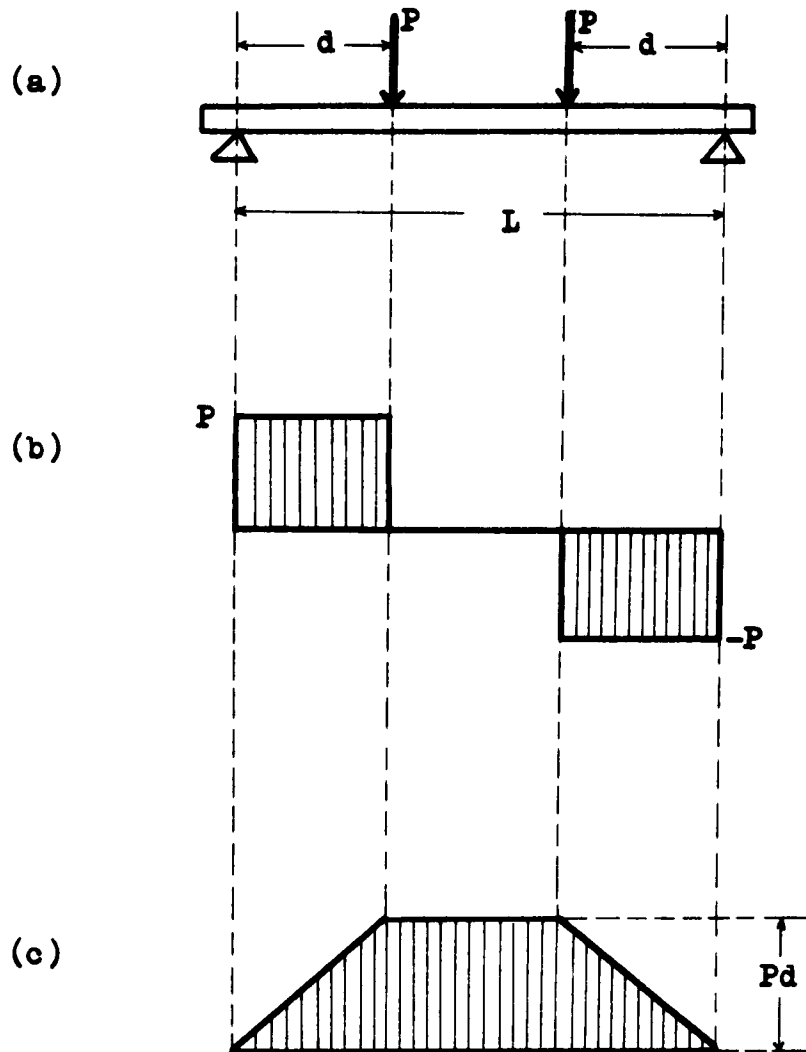


Figure 10. Schematic representation of MOR test:
 (a) Four-point bend test
 (b) Shear diagram for four-point bend test
 (c) Moment diagram for four-point bend test

EXPERIMENTAL PROCEDURE

Selection of the Composition

Three different mixtures of powders were prepared for the selection of the ceramic composition for the bone implants. They are summarized in Table 5a.

Table 5a. Powder compositions tested for the implants

Compound	Composition					
	I		II		III	
	w/w	mol%	w/w	mol%	w/w	mol%
$\text{Ca}_3(\text{PO}_4)_2$	57.5	28.5	60.4	31.4	56.9	28.3
CaF_2	4.8	9.4	—	—	—	—
MgCO_3	17.1	31.1	17.9	34.3	16.9	30.9
Al_2O_3	20.6	31.0	21.7	34.3	20.4	30.8
Na_3AlF_6	—	—	—	—	1.0	0.7
TiO_2	—	—	—	—	4.8	9.3

Compositions II and III were tested for tooth root implants at Iowa State University before (References 24 and 25). After firing, a whitlockite-spinel composite was obtained for both composition II and composition III. However, composition III contained impurities like Na_3AlF_6 and

TiO₂ for processing and solubility reasons.

One kilogram lots of each composition were weighed and then ball milled with water for 14 hours. After milling the material was dried on a plaster bat and then broken into chunks and dried in an oven at 110 C. Each mixture was ground by mortar and pestle to pass through a 20 mesh sieve, then mixed with 5% methyl cellulose solution (about 10 cc of solution was used for each 100 grams of powder) and pressed at 5000 psi with a Carver Laboratory Press (Model C) in the form of small pellets (1/2 in. in diameter and approximately 1 in. in height), and finally, the pellets were pressed isostatically at 30,000 psi.

The test pellets were calcined at 1000 C in a Lindberg Hevi-Duty furnace for half an hour and they were left to cool in the furnace. Density and porosity calculations were made after water-immersion tests. The following equations were used for the calculation of density and porosity:

$$\text{Density} = \frac{W_f}{W_{st} - W_{ss}} \quad \text{Eq. 34a}$$

$$\text{Porosity} = \frac{W_{st} - W_f}{W_{st} - W_{ss}} \times 100 \quad \text{Eq. 34b}$$

where W_f is the weight after firing, W_{st} is the weight after saturating the specimen with water and W_{ss} the weight measured while the saturated specimen is suspended in water.

All the pellets that were fired at 1000 C contained 40-50% porosity; therefore, it was obvious that higher firing temperatures were required to produce dense pellets.

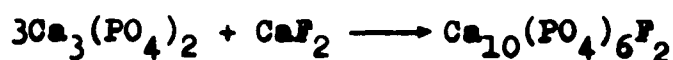
Pellets of the three compositions fired at temperatures between 1350 C to 1500 C in a large Globar furnace all cracked except for those of composition I, even if very slow heating procedures were employed (approximately 45 C/hr).

Some of the pellets which cracked were coated with gold (200 Å thick), and studied by scanning electron microscope to determine the reason for cracking. Also, thermal expansion measurements were made on the fired pellets of composition II. The data were obtained by using an X-Y recorder with a LVDT system. The specimens were heated up to 1000 C and then, they were left to cool in the furnace. The temperature versus the expansion/contraction of the specimen was plotted by the recorder. The linear thermal expansion coefficient of the whitlockite-spinel composite was calculated to be $16.7 \times 10^{-6} \text{ C}^{-1}$. In the literature, the linear expansion coefficient of

spinel is given as $7.6 \times 10^{-6} \text{ C}^{-1}$ (43). Therefore, the higher value obtained in this study must be due to the presence of whitlockite in the ceramic. This suggests that the thermal expansion coefficient of whitlockite is much larger than that of spinel. Therefore, the cause of cracking observed in whitlockite-spinel ceramics must be due to the mismatch of the expansion coefficients, which sets up boundary stresses between the grains of the two phases and leads to fracture.

The thermal expansion coefficient of 2% Nd-doped fluorapatite is given as $10.0 \times 10^{-6} \text{ C}^{-1}$ along the c direction and $9.4 \times 10^{-6} \text{ C}^{-1}$ along the a direction (36). This shows that there is a better match between the expansion coefficients of fluorapatite-spinel composite than the expansion coefficients of whitlockite-spinel composite. Therefore, the ceramics of composition I containing fluorapatite and spinel did not crack.

Due to the problems encountered in producing sound specimens from compositions II and III, it was decided that only composition I was going to be used for the bone implants. During firing, whitlockite and calcium fluoride react to form fluorapatite, and magnesium carbonate combines with alumina to form the spinel according to the following reactions:



Specimen Preparation

Specimen preparation for x-ray diffraction

The pellets for x-ray diffraction studies were pressed at 5000 psi from -20 mesh powder (of composition I & II) in a 1/2 in. or 3/4 in. diameter steel die to 1 in. in height without adding any methyl cellulose solution, and then they were pressed isostatically at 30,000 psi. The pellets were fired in a Globar furnace controlled by a Trendtrak programmer. The heating rate was such that the temperature reached 1000 C in 10 hours, and stayed at 1000 C for 4 hours, then increased to 1485 C in 4.5 hours, and stayed at 1485 C for 1.5 hours. However, some pellets were fired at 1425 C and 1450 C as well as 1485 C for x-ray diffraction studies to see the effect of temperature on the composition.

Specimen preparation for optical microscopy, bend test and solubility test

Porous specimens were prepared as well as the non-porous specimens for all these tests. Graded naphthalene crystals (between 20 and 65 mesh, or 208 μm to 833 μm

in size) were mixed with the powder in the right proportions to produce the desired interconnected porosity, and then pressed at 5000 psi in a 1/2 in. diameter die to produce 1 in. tall pellets; or they were pressed at 6800 psi in a 5/16 in. by 4 in. rectangular die to produce 1/2 in. wide bars. After isostatic pressing at 30,000 psi, they were fired at 1485 C for optical microscopy and solubility studies, and at 1425 C, 1450 C and 1485 C for the bend test using the same heating procedure described before.

In order to reduce shrinkage, some bars were pressed from grog, i.e., the powder obtained from a ceramic that was already fired once. Fines of green powder (-250 mesh) were added to the -20 mesh grog which was already mixed with methyl cellulose solution. Naphthalene additions were made to increase the porosity. The bars made from grog were pressed at 6800 psi and then isostatically at 30,000 psi. They were fired up to 1450 C in the Trendtrak controlled Global furnace using the same heating procedure described earlier.

X-Ray Diffractometer Studies

The pellets of fluorapatite-spinel fired at different temperatures ranging from 1400 C to 1485 C were crushed and ground into powder, and their diffraction patterns

were obtained from the Siemens X-ray Diffractometer using $\text{CuK}\alpha$ radiation. The d values of the peaks (interplanar spacings of the diffracting planes) were calculated from Bragg's law, i.e., $\lambda = 2d \sin\theta$, where λ is the wavelength of the $\text{CuK}\alpha$ radiation and equals 1.5418 \AA , and θ is the half-angle between the incident and the diffracted beam. The calculated d values are compared with those given in the "ASTM Inorganic Index to the Powder Diffraction File" (60) to find the matching set of d values and thus, identify the compounds present in the ceramic.

Optical Microscope Studies on Fluorapatite-Spinel Specimens

The pellets of fluorapatite-spinel ceramic fired at 1485 C were ground using 320, 400 and 600 grit SiC paper, successively, and then polished with $6 \mu\text{m}$ and $1 \mu\text{m}$ diamond paste on nylon cloth using lapping oil as the lubricant. The pellets were washed with soap and water and then polished with $0.3 \mu\text{m}$ alpha alumina and $0.05 \mu\text{m}$ gamma alumina, successively. Lecloth[®] (flocked cotton sateen) was used as lap covering with distilled water as lubricant.

The polished pellets were etched by 2% Nital (2 ml HNO_3 in 100 ml 95% methanol) for about 1 minute. The grain structure, and the size and the distribution of pores

were studied with the Olympus Inverted Stage Optical Microscope.

Study of the Bending Strength

The three-point bend test was used to determine the moduli of rupture (MOR) of the rectangular bars, both porous and nonporous. The effect of the firing temperature on MOR was determined on bars ranging from approximately 0% porosity to 60% porosity, and were fired at 1425 C, 1450 C, and 1485 C. The desired amount of porosity was obtained by adding graded naphthalene crystals to the powder mixture.

The MOR of bars fired at 1450 C and containing grog were also determined.

The effect of exposure to physiological solutions on MOR was evaluated from in-vitro tests in Ringer's solution¹. Bars of approximately 0%, 40%, and 50% porosity were fired at 1485 C and then cut in half. One half of each bar was used as the control and the other half was left in Ringer's solution for 4, 5, 6, 8 or 10 months. The MOR of the control bars and the MOR of the bars left in Ringer's solution were determined in three-point bend test, and the change in MOR for each bar was calculated.

¹The composition of Ringer's solution is given in Appendix A.

Four smaller bars (0.106 X 0.240 X 1 in.) fired at 1485 C were implanted subcutaneously in a dog for 7.5 months and then removed and tested for MOR. Five control bars of similar size and subjected to the same autoclave sterilization were also tested in three-point bend test to determine the change in MOR. All the subcutaneous bars and the control bars were rounded off on the sharp edges to decrease the possibility of irritation to the tissues.

The MOR tests were performed using an Instron Universal Testing Instrument (Model: TTOML). The bend test fixtures were made of tool steel and the load was applied through pins of 0.125 in. in diameter. The bottom fixture was made of two pieces that stayed on a pin of 0.125 in. in diameter (Fig. 11). The two pieces were held together by a rubber band. The test speed was 0.01 cm/min and 500 kg tension/compression load cell was used. The modulus of rupture was calculated from the following equation:

$$\text{MOR} = \frac{3}{2} \frac{PL}{bd^2} \quad \text{Eq. 33}$$

where P=load (lb), L=span length (0.700 in. in this case), b=width of the specimen (in.), and d=depth of the specimen (in.).

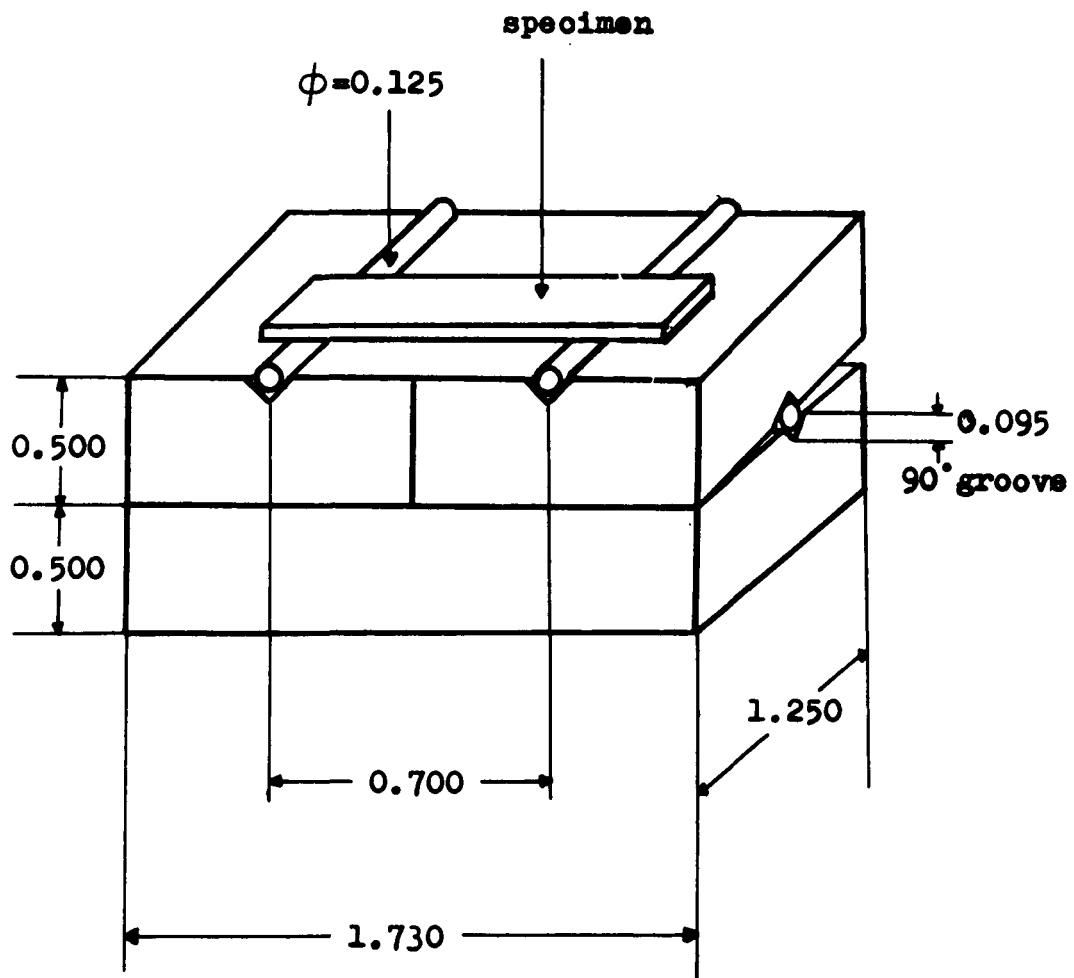


Figure 11. The bottom fixture used in the three-point bend test (Dimensions are in inches)

Scanning Electron Microscope Studies

A carbon coated (300 Å thick) pellet fired at 1600 C and containing approximately 30% porosity was examined in SEM using x-ray analysis in order to see the distribution of calcium, phosphorus, magnesium and aluminum. Tracor Northern TN 2000 X-ray analyzer was used to analyze up to 25,000 counts for each element. The grain structure inside a pore, and the distribution of the elements are shown in the results section.

The fracture surfaces from a porous bar (ca. 40% porosity) and a nonporous bar were coated by gold (225 Å thick) and they were examined by SEM (Model: JSM -U3).

Solubility Studies

The weights of the bars were measured before placing them in Ringer's solution, and they were remeasured after removal from the solution upon drying in an oven at 110 C. They were cleaned ultrasonically for 1 hour, and then their weights were measured again.

The solution the bars stayed in for 10 months was analyzed for any dissolved F^- or Al^{3+} . The ultrasonic cleaning water of the bars which were exposed to Ringer's solution for 10 months was analyzed for F^- and Al^{3+} , as well as for Na^+ , K^+ , SO_4^{2-} , PO_4^{3-} , inorganic carbon, Ca^{2+} , Mg^{2+} and Cl^- , which were the ions of the salts

present in Ringer's solution.

Soft Tissue Reaction Test

Four small nonporous bars (0.106 X 0.240 X 1 in.) fired at 1485 C and sterilized were implanted subcutaneously in the back of a dog to study the soft tissue reactions. They were removed after 7.5 months to see if there was any fibrous tissue formation around them, or any dissolution marks were visible. The bars were tested in the three-point bend test to detect any strength changes after exposure to tissue fluids.

Implants

Three types of implants were designed and produced from the fluorapatite-spinel ceramic: porous bone bridges for dogs, partially porous canine tooth roots for dogs, and nonporous tooth roots for monkeys. The shapes and dimensions of these implants are shown in Fig. 12, Fig. 13, and Fig. 14. However, the monkey tooth roots have not been implanted and although one canine root for dog was implanted, it fell out after about a week because it was too big for the socket, so it was not pushed in until the gingiva could be closed above it.

Bone bridges of two different sizes and porosities were implanted in two dogs. The first one was removed

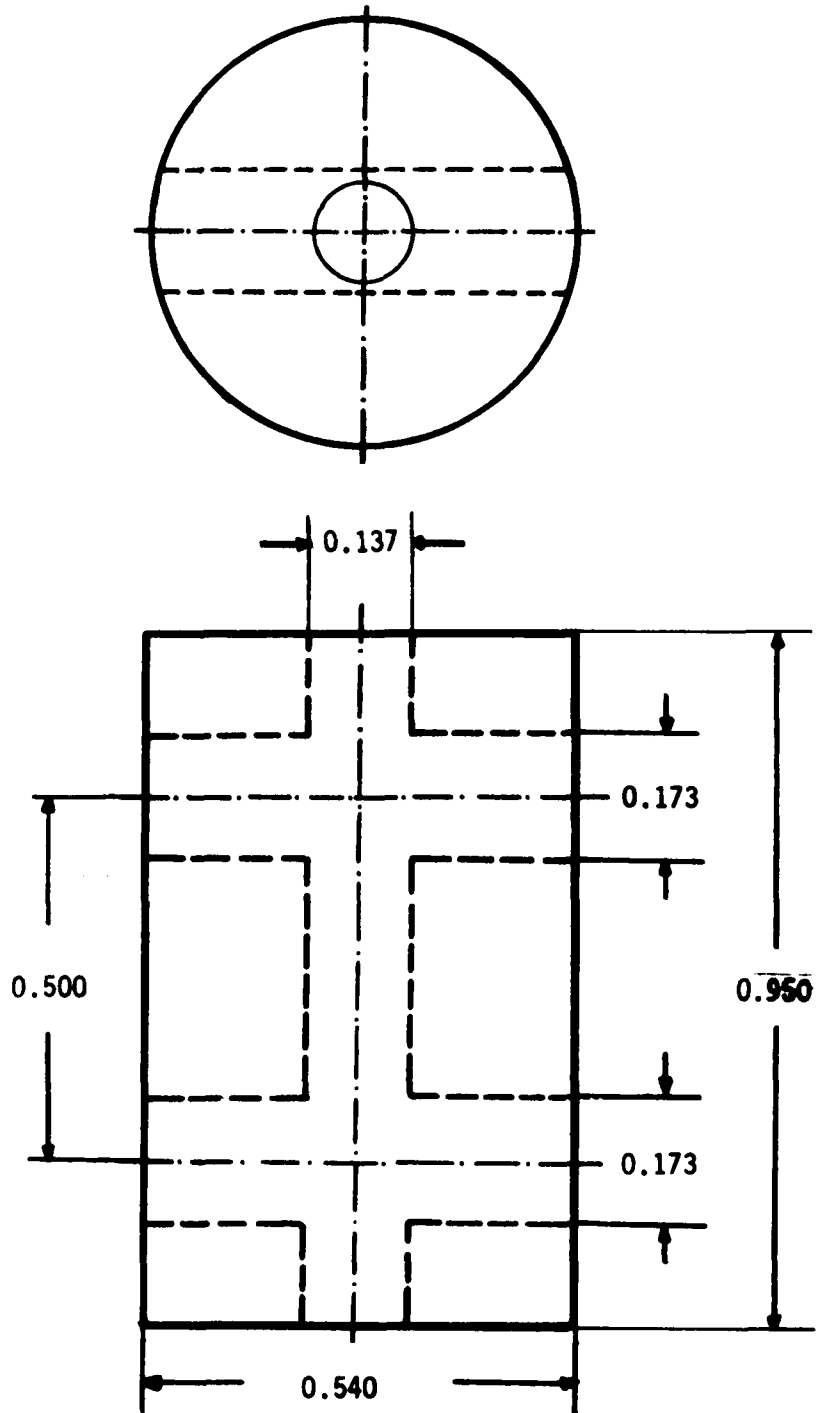


Figure 12. Porous bone bridge for dogs. The dimensions (in inches) may vary according to application

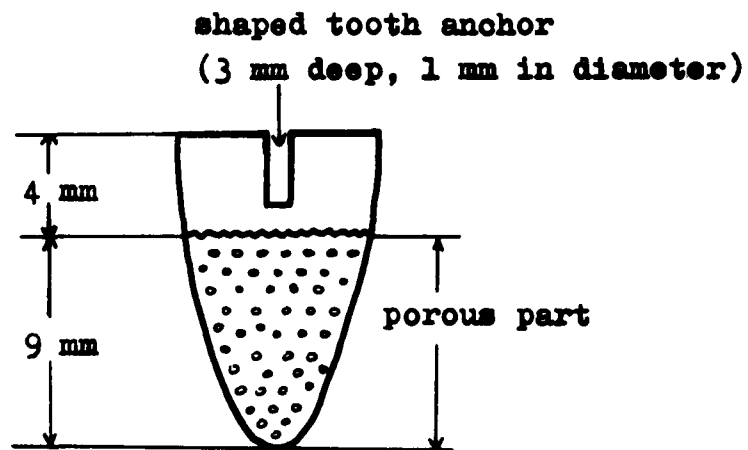
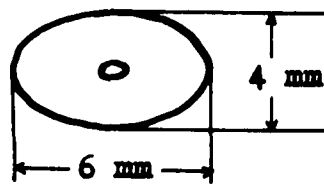


Figure 13. Tooth root for the canine in dogs

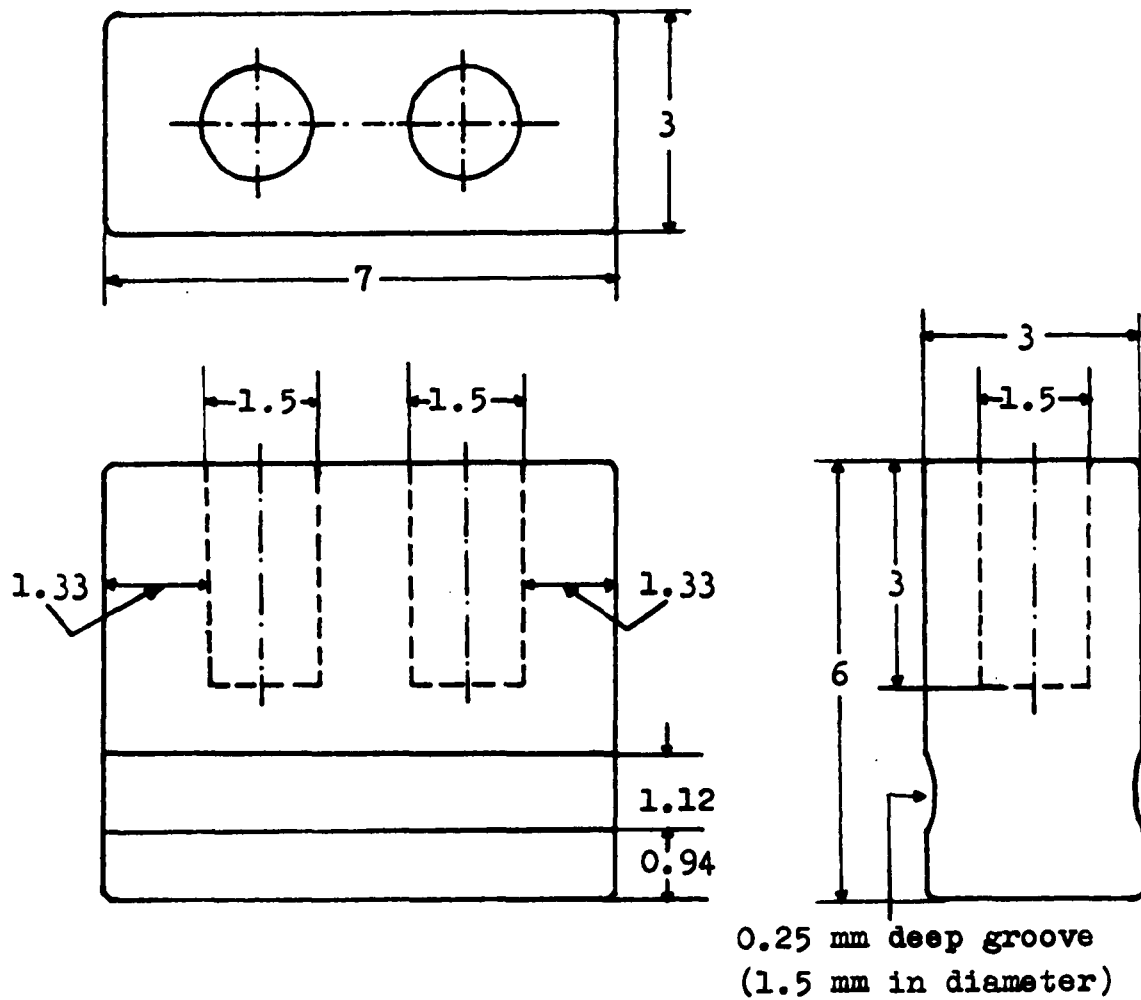


Figure 14. Tooth root for monkey. The dimensions are in millimeters

after 11 months and the second bone bridge has been in place since June 1980, although the steel bone plate was removed 15 months later.

The first bone bridge contained 50% porosity, and the weight percentages of grog (-20 mesh), green powder (-250 mesh) and naphthalene (-20 mesh) were 62.5%, 12.5%, and 25%, respectively. It was fired at 1450 C for 1 hour in a Trendtrak controlled globar furnace. The axial hole and the two transverse holes for the screws were drilled after firing. The bone bridge was refired up to 1200 C to burn off any organic residues left after machining. It was sterilized in an autoclave before implantation. Its final dimensions were 0.718 in. in diameter and 0.974 in. in length with an axial hole of 0.270 in. in diameter. The bend strength of an equivalent rectangular bar was found to be 813 ± 43 psi. A picture of the bone bridge, just before implantation, with the 316 stainless steel bone plate attached to it is shown in Fig. 15.

The second bone bridge contained 30% porosity obtained by adding -20 mesh naphthalene crystals to the powder before pressing. It contained no grog in contrast to the first bone bridge. The bend strength of an equivalent bar was 2195 ± 296 psi. It was fired up to 1450 C as was the first bone bridge, and then refired up to 1200 C.

**Figure 15. The first bone bridge with the
steel bone plate attached to it**



after machining of the holes. The final dimensions were: 0.850 in. diameter, 0.955 in. height with an axial hole of 0.240 in. in diameter.

The surgeries were performed using antiseptic surgical procedures. Radiographs of the dogs were taken before and after the surgeries, and at regular intervals during the follow-up period.

Microscopic Analysis of the Recovered Implant

The first bone bridge was removed after 11 months. It was fixed in 10% buffered formalin with its surrounding tissues (minimum of 48 hours is required). It was dehydrated in 30%, 60% and 90% acetone, successively, keeping it in the solution for one day each time. It was kept in 100% acetone for three days changing the solution daily.

After dehydration, the bone bridge was embedded in Araldite resin mixed with DDSA, NMA and DMP-30 according to the instructions¹. The resin was added onto the implant in vacuum (5 cm of Hg) in order to achieve complete infiltration of the tissues with the resin. After leaving the embedded implant at room temperature for one day, it was cured in an oven at 35 C overnight, at 45 C the following

¹For 100 ml of embedding material, 57.5 ml Araldite 506 was mixed with 13.3 ml DDSA, 29.2 ml NMA and 2ml DMP-30 accelerator. Manufacturer: Ernest F. Fullam, Inc.; Schenectady, New York.

day and at 60 C overnight. The hardened block of the implant and resin was sectioned into thin sections using a low-speed diamond saw. The thin sections were ground on one side using 360, 400 and 600 grit SiC paper, successively, and mounted in etched-well glass slides using a transparent cement. The unpolished surface was ground to a thickness of approximately 40 microns, in the same way as described above.

The glass slides of the implant-tissue samples were examined using polarized transmitted light in the Ultraphot II light microscope. Color Polaroid pictures were taken using the camera attached to the microscope.

RESULTS AND DISCUSSION

X-Ray Diffraction

The fired ceramic of composition I showed the presence of fluorapatite, $\text{Ca}_{10}(\text{PO}_4)_6\text{F}_2$, and spinel, MgAl_2O_4 . The diffraction peaks were sharper for the ceramics fired at 1485 C than the peaks for the ceramics fired at 1425 C or 1450 C. Ceramics of composition II contained whitlockite, $\text{Ca}_3(\text{PO}_4)_2$, and spinel, MgAl_2O_4 , according to the x-ray diffraction analysis. The x-ray data for composition I and composition II are given in tables 5b and 5c, respectively.

Optical Microscopy

The grain structure and the distribution of pores of the fluorapatite-spinel ceramic containing about 30% porosity can be seen in figures 16, 17 and 18. In Fig. 16, the matrix is fluorapatite and the unetched crystals are spinel. Figures 17 and 18 show two different regions of the same ceramic at a lower magnification. In Fig. 17, the average pore size is about $400 \mu\text{m}$, whereas in Fig. 18, some of the pores are about $800 \mu\text{m}$.

Bending Strength

The results of the three-point bend tests on ceramics fired at 1425 C and 1450 C are shown in Fig. 19 as a function of porosity. The effect of firing temperature

Table 5b. Interplanar spacings corresponding to the diffraction pattern of composition I (* indicates the peaks that were actually present in the diffraction pattern)

FLUORAPATITE (41)				SPINEL (40)	
d Å	I/I ₁	d Å	I/I ₁	d Å	I/I ₁
8.12	8	*1.837	30	*4.67	4
5.25	4	*1.797	16	*2.858	40
4.684	1	*1.771	14	*2.436	100
4.055	8	*1.748	14	2.333	3
3.872	8	*1.722	16	*2.021	58
3.494	1	1.684	1	1.649	10
*3.442	40	1.637	6	*1.555	45
*3.167	14	1.607	4	*1.429	58
*3.067	18	1.580	2	1.366	3
*2.800	100	1.562	1	1.278	2
*2.772	55	1.534	6	*1.232	9
*2.702	60	1.524	4	1.218	1
*2.624	30	1.501	4	1.1662	7
2.517	6	1.497	4	1.1312	2
2.289	8			1.0796	4
*2.250	20			1.0518	12
2.218	4			1.0100	5
2.140	6			0.9522	3
2.128	4			0.9330	10
2.061	6			0.9034	6
2.028	2			0.8869	1
1.997	4			0.8613	1
*1.937	25			0.8469	10
1.884	14			0.8247	20
1.862	4				

Table 5c. Interplanar spacings corresponding to the diffraction pattern of composition II (* indicates the peaks that were actually present in the diffraction pattern)

WHITLOCKITE (61)				SPINEL (40)	
d Å	I/I ₁	d Å	I/I ₁	d Å	I/I ₁
8.15	12	2.499	6	4.67	4
*6.49	16	2.407	10	*2.858	40
6.22	6	2.375	6	*2.436	100
*5.21	20	2.263	10	2.333	3
4.80	2	2.249	4	*2.021	58
4.39	8	2.241	2	1.649	10
4.15	4	2.195	14	*1.555	45
*4.06	16	*2.165	12	*1.429	58
4.00	4	2.103	4	1.366	3
*3.45	25	2.076	8	1.278	2
3.40	4	2.063	4	*1.232	9
*3.36	10	2.061	6	1.218	1
3.25	8	2.033	10	1.1662	7
*3.21	55	2.023	6	1.1312	2
3.11	2	2.017	4	1.0796	4
3.01	16	2.000	8	1.0518	12
*2.880	100	1.970	2	1.0100	5
*2.757	20	1.946	4	0.9522	3
*2.710	10	*1.933	20	0.9330	10
*2.674	8	*1.895	16	0.9034	6
*2.607	65	1.879	14	0.8869	1
2.562	6	1.830	12	0.8613	1
2.553	8	1.812	6	0.8469	10
*2.520	12	1.798	6	0.8247	20

Figure 16. Microstructure of the fluorapatite-spinel ceramic. The field diaphragm of the Olympus Inverted Stage Microscope is seen in view. It was used to improve the contrast between the two phases. The matrix is fluorapatite and the unetched crystals are spinel. Magnification: 1000X

Figure 17. Polished surface of the same ceramic at 50X. Average pore size is about $400\mu\text{m}$ in this region

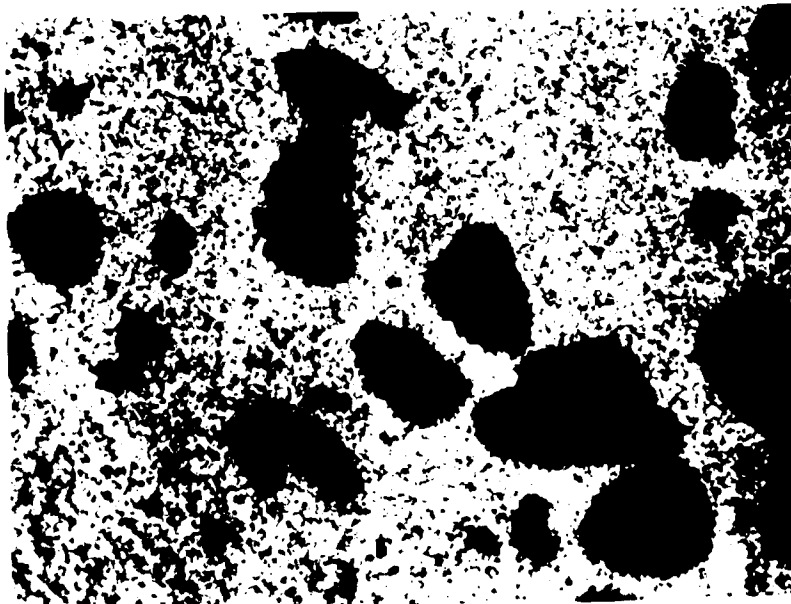


Figure 18. Polished surface of the fluorapatite-
spinel ceramic at 80X. Some of the pores
are about $800\mu\text{m}$ in this region



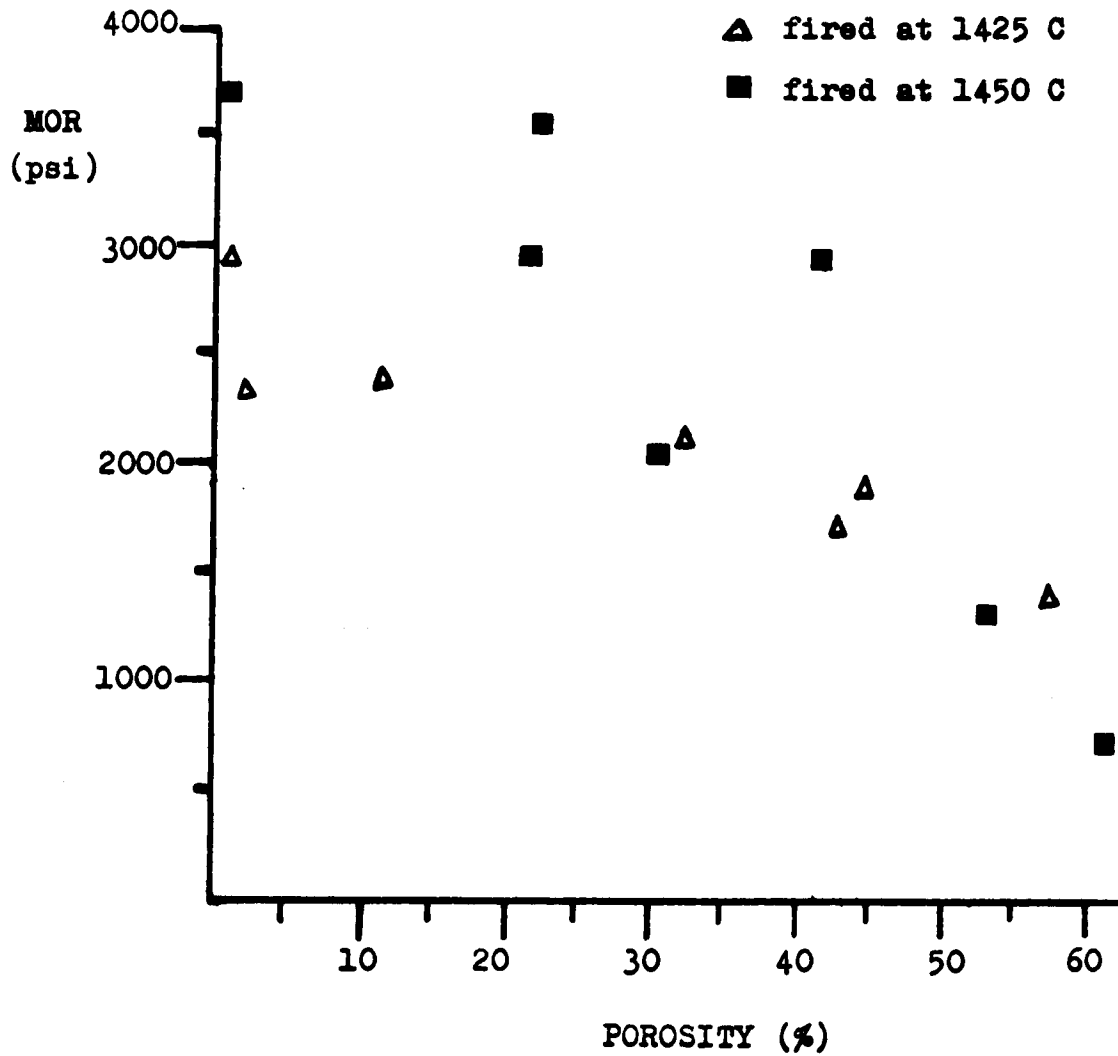


Figure 19. Variation of bend strength with porosity for the ceramics fired at 1425 C and 1450 C

on bend strength was more pronounced in specimens containing less than 20% porosity. This means that porosity has greater influence on bend strength than the firing temperature for specimens containing 30% or more porosity. A comparative plot of MOR versus porosity is given in Fig. 20 for the ceramics fired at 1450 C and 1485 C. The difference in MOR of the ceramics fired at different temperatures becomes larger with decreasing porosity, as can be seen from Fig. 20.

The MOR plot of bars containing grog is shown in Fig. 21 as a function of porosity. The firing temperature for these bars was 1600 C.

As can be seen from these figures, bend strength decreases almost exponentially with increasing porosity.

The effect on MOR of the exposure of the ceramic to Ringer's solution is summarized in Table 5d. The method of evaluating the statistical significance of the observed differences between the MOR of the control bars and the MOR of the bars exposed to Ringer's solution, is explained in Appendix B. The MOR data vary from bar to bar within each group (i.e., the group of bars that was exposed to Ringer's solution as well as the group of bars that was not exposed); therefore, the two groups are not independent. In this case, direct comparison of the mean MOR of the

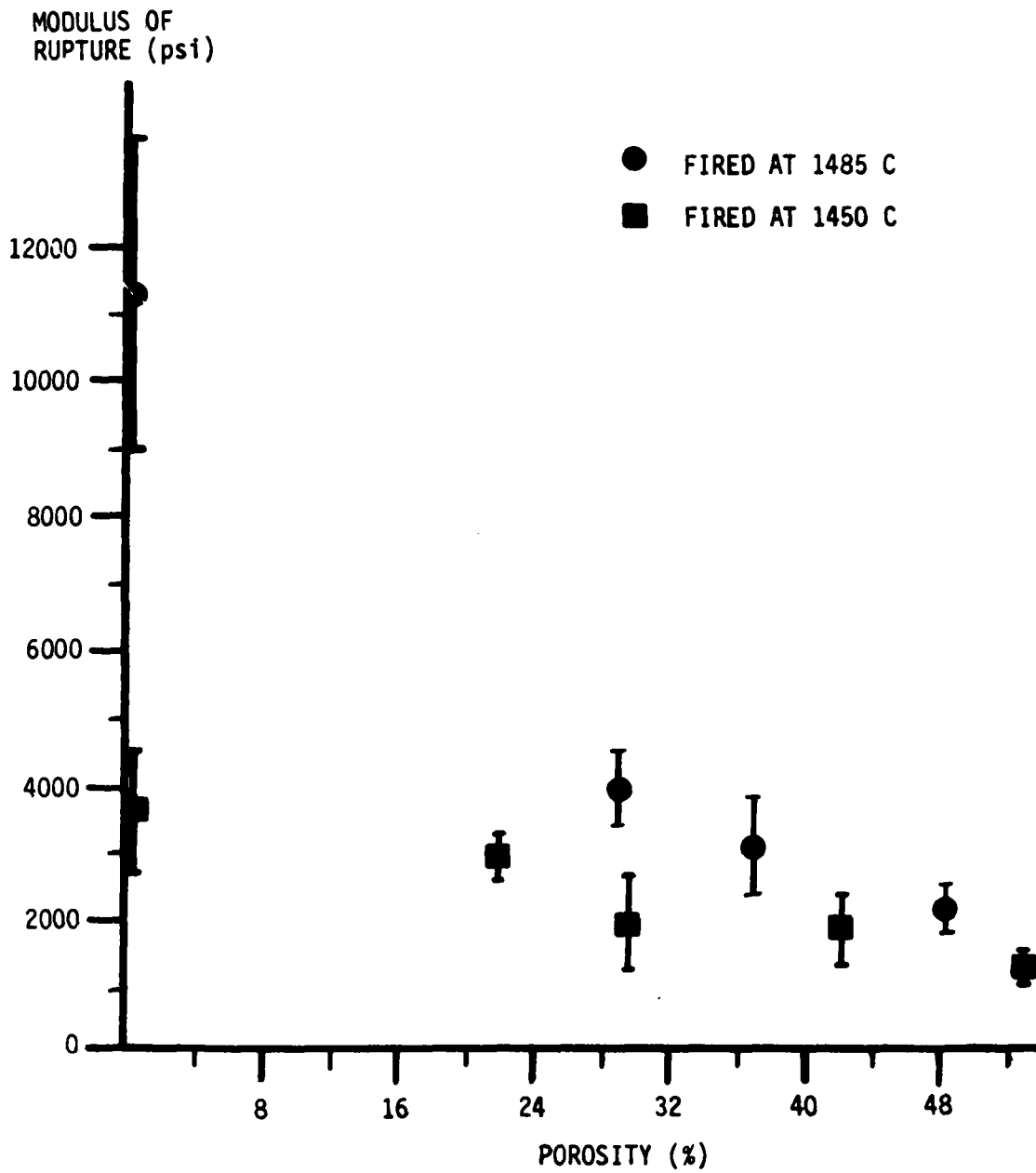


Figure 20. Variation of bend strength with porosity for the ceramics fired at 1450 C and 1485 C. Brackets indicate standard deviations

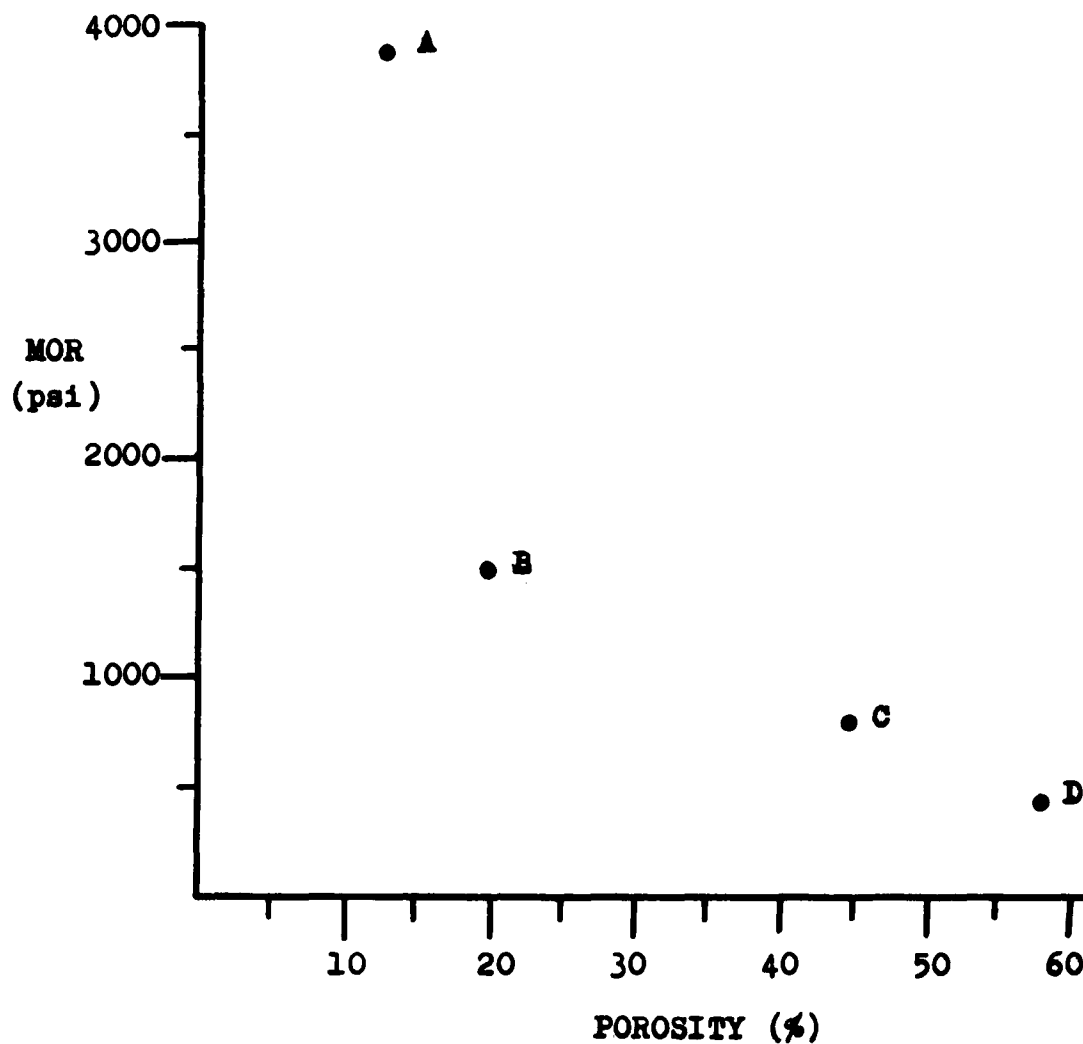


Figure 21. The MOR of bars containing grog (firing temperature: 1450 C)
A: Contained 80% grog, 20% fine powder, and no naphthalene
B: 85% grog, 15% fine powder, and no naphthalene
C: 63% grog, 12% fine powder, and 25% naphthalene
D: 40% grog, 20% fine powder, 40% naphthalene

Table 5d. MOR change due to the exposure of the ceramic to Ringer's solution. (P=porosity, L=length of exposure, n=number of samples, \bar{X} =mean difference between the MOR of exposed and unexposed halves of ceramic bars, S=standard deviation of \bar{X} , $|t|_{\text{calc}}$ =absolute value of t calculated from Eq. 35, $t_{0.05}$ =theoretical value of t when the probability of a larger value is 5%)

P (%)	L (months)	n	\bar{X} (psi)	S (psi)	$ t _{\text{calc}}$	$t_{0.05}$
0	10	3	491	3067	0.277	4.303
0	8	4	4978	4770	2.087	3.182
0	6	5	2133	1876	2.542	2.776
0	5	5	1926	4025	1.070	2.776
0	4	5	359	4785	0.168	2.776
0	0 ^a	2	589	64	13.097	12.706
30	10	3	-1528	389	6.804	4.303
40	10	4	-1177	489	4.814	3.182
40	8	5	-383	692	1.238	2.776
40	6	4	-921	206	8.942	3.182
40	5	5	-883	359	5.500	2.776
40	4	5	-1033	628	3.678	2.776
40	0 ^a	5	339	279	2.717	2.776
50	8	5	-136	321	0.947	2.776
50	6	5	-605	282	4.797	2.776
50	5	5	-303	332	2.041	2.776
50	4	5	-305	581	1.174	2.776
50	0 ^a	3	357	311	1.988	4.303

^aNeither half of these bars was exposed to Ringer's solution.

groups with each other will lead to erroneous results. The correct procedure is to compute the individual differences (i.e., the change in MOR of each bar when half of it was exposed and the other half was not), and then test whether the mean difference is significantly different from zero. This reduces the problem of paired data to a single sample problem in which the significance of the deviation of the mean difference from zero can be tested by Student's t test, which is explained in Appendix B.

Table 5d suggests that all of the 40% porous bars, except for the group that was exposed for 8 months, have statistically important decrease in MOR. Also, the group containing 50% porosity and exposed for 6 months, and the group containing 30% porosity and exposed for 10 months (it was the only group containing 30% porosity) appear to have significant reductions in their MOR values. However, a check for the test was made by comparing the bars neither half of which was exposed. As can be seen from Table 5d, a statistically significant difference between the MOR of the halves of the unexposed nonporous bars seemed to exist. This suggests that the results obtained from the t test may not be accurate due to the several factors like the inhomogeneous distribution of porosity within the same bar, or experimental errors in

the MOR test like surface irregularities or misalignment of the bar in between the load-applying pins.

The change in MOR of the subcutaneous bars was determined by using a different equation for the t test, because the bars were not paired in this case. This method is explained in Appendix C. The results of this test are summarized in Table 6.

Table 6. The effect of tissue fluids on MOR of non-porous bars

	Control bars	Subcutaneous bars
n	5	4
\bar{X} (psi)	16874	15441
S (psi)	1293	3633
$ t _{calc}$		0.831
$t_{0.05}$		2.365

n: number of bars tested in each group

\bar{X} : the average MOR for each group

S: the standard deviation of the MOR

$|t|_{calc}$: absolute value of t calculated from the data

$t_{0.05}$: the value of t for 95% confidence limit

As can be seen from Table 6, tissue fluids do not seem to affect the MOR of the subcutaneous bars that were exposed for 7.5 months.

The number of specimens used in the MOR test to determine the effect of porosity and the effect of exposure to physiological solutions on strength of the fluorapatite-spinel ceramic was too small (less than or equal to 5) to apply Weibull's statistical theory of fracture, which predicts that larger samples should be weaker and that the dispersion in values of fracture stress should increase as the median strength increases. However, the MOR versus porosity data for the ceramics fired at 1485 C were obtained from approximately 25 specimens for each data point (Fig. 20). As predicted by the statistical theory of fracture, the standard deviations increase as the average MOR become larger for this group of specimens.

Ringer's solution is similar to the physiological fluids; therefore, the MOR change upon exposure of the ceramic to Ringer's solution is important in predicting the service life of the ceramic. However, the ceramics tested in vitro were not under any kind of stress. Therefore, static fatigue tests should be performed on the fluorapatite-spinel ceramic for future study. Physiological environment is expected to increase the crack velocity and lead to fracture at shorter times than those predicted

for the ceramics that were not exposed to the solution. For ceramics, the behavior under cyclic stress conditions can be explained in terms of crack-growth mechanisms operating under static conditions, with the relevant time parameter being the sum of the times which the specimen spends under tensile stress. Therefore, dynamic fatigue tests should not be required for the fluorapatite-spinel ceramic. The failure of the two implants in vivo emphasizes the need for static fatigue tests for this ceramic. Firing temperatures higher than 1485 C should also be tested for future study to improve the strength.

Scanning Electron Microscope Studies

Figure 22 shows the SEM picture of a carbon coated 30% porous pellet inside a pore. The long, large crystals are fluorapatite, and the small crystals are spinel. The distribution of Ca, P, Mg, and Al is obtained by x-ray analysis in SEM (Fig. 23 - Fig. 26). Mg and Al areas overlap, but they are separated from the Ca and P regions, which means that there is no solubility of Mg or Al in fluorapatite. Figure 27 shows the SEM picture of a whitlockite-spinel ceramic for comparison of grain structure. The fracture surface after the bend test of the fluorapatite-spinel ceramic is shown in figures 28 through 31. The fracture in this ceramic appears to be of

Figure 22. SEM picture of a 30% porous fluorapatite-spinel ceramic inside a pore. The long, large crystals are fluorapatite, and the small crystals are spinel. The ceramic was fired at 1600 C (2000X)

Figure 23. Calcium distribution in the 30% porous fluorapatite-spinel ceramic fired at 1600 C. The specimen was scanned up to 25,000 counts at 15 kV (2000X)

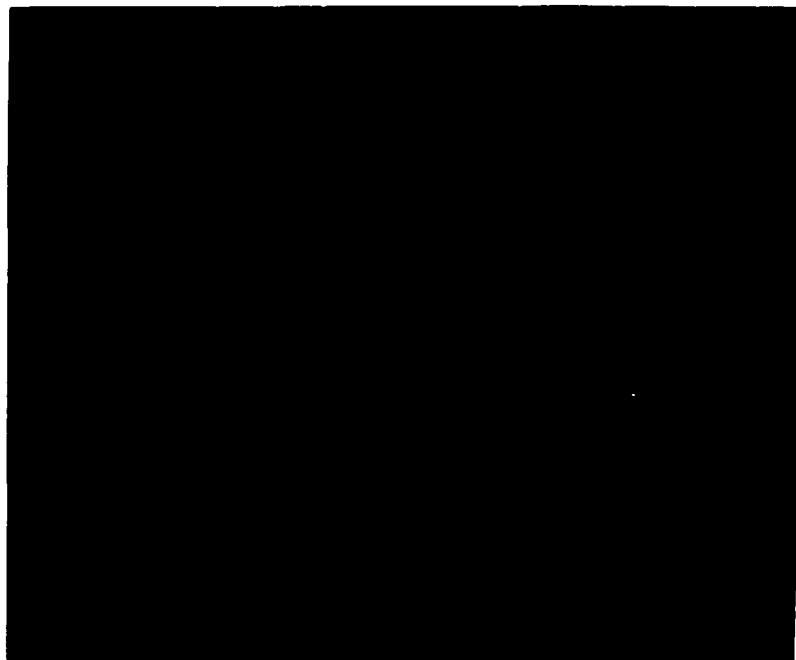


Figure 24. Phosphorus distribution in the 30% porous fluorapatite-spinel ceramic fired at 1600 C. The specimen was scanned up to 25,000 counts at 15 kV (2000X)

Figure 25. Magnesium distribution in the 30% porous fluorapatite-spinel ceramic fired at 1600 C. The specimen was scanned up to 25,000 counts at 15 kV (2000X)

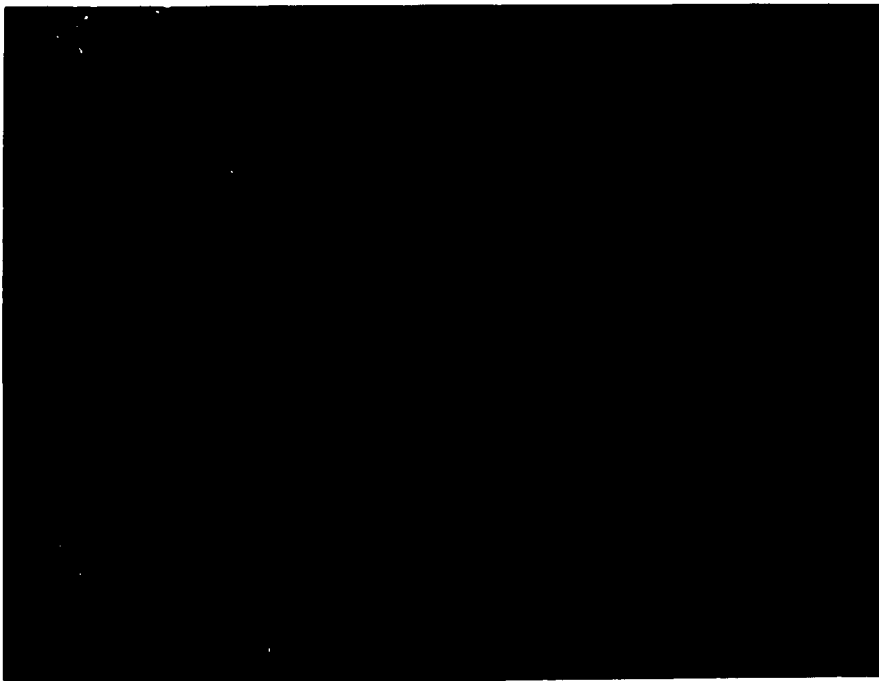
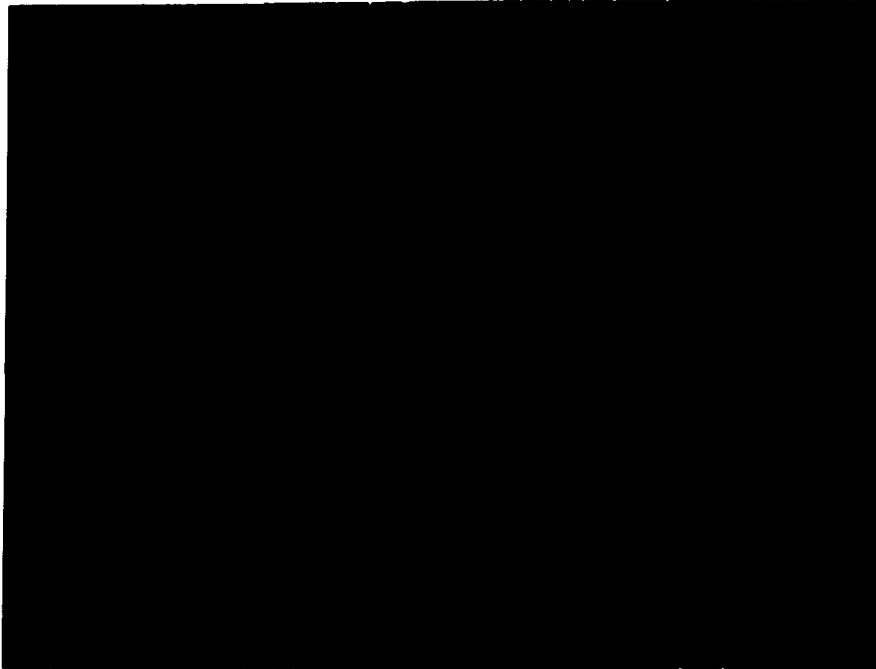


Figure 26. Aluminum distribution in the 30% porous fluorapatite-spinel ceramic fired at 1600 C. The specimen was scanned up to 25,000 counts at 15 kV (2000X)

Figure 27. SEM picture of a whitlockite-spinel ceramic fired at 1150 C. The fired surface in a pore shows crystals of hexagonal whitlockite and cubic spinel (1000X)

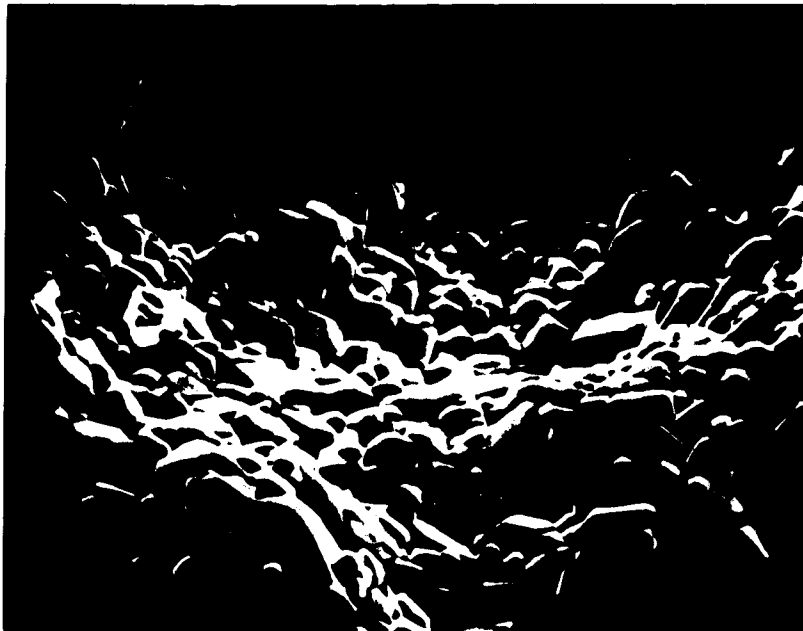
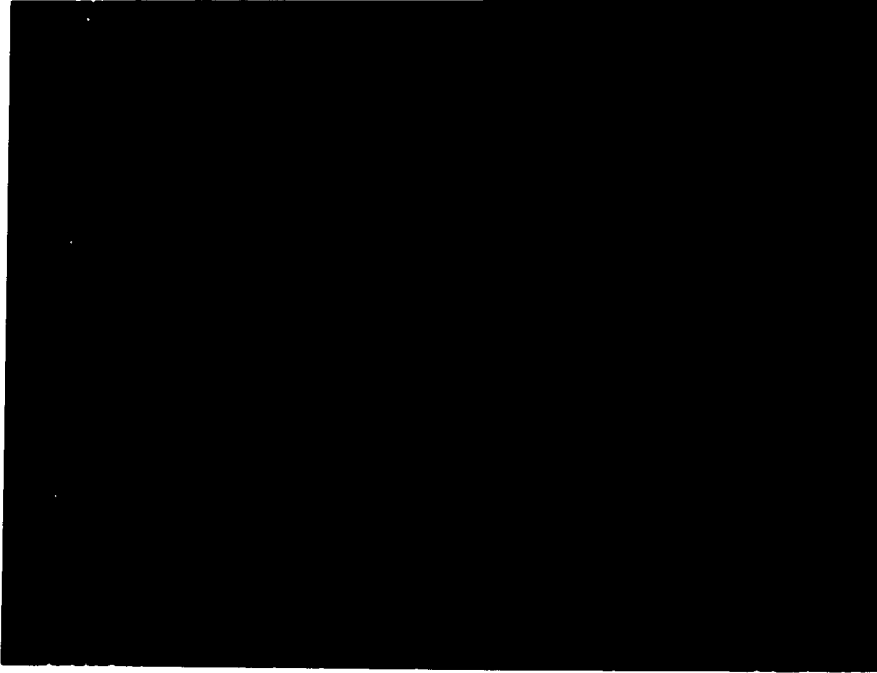


Figure 28. Interface of a pore and the fracture surface in a 40% porous fluorapatite-spinel ceramic fired at 1485 C (300X)

Figure 29. Interface of a pore and the fracture surface in a 40% porous fluorapatite-spinel ceramic fired at 1485 C (3000X)

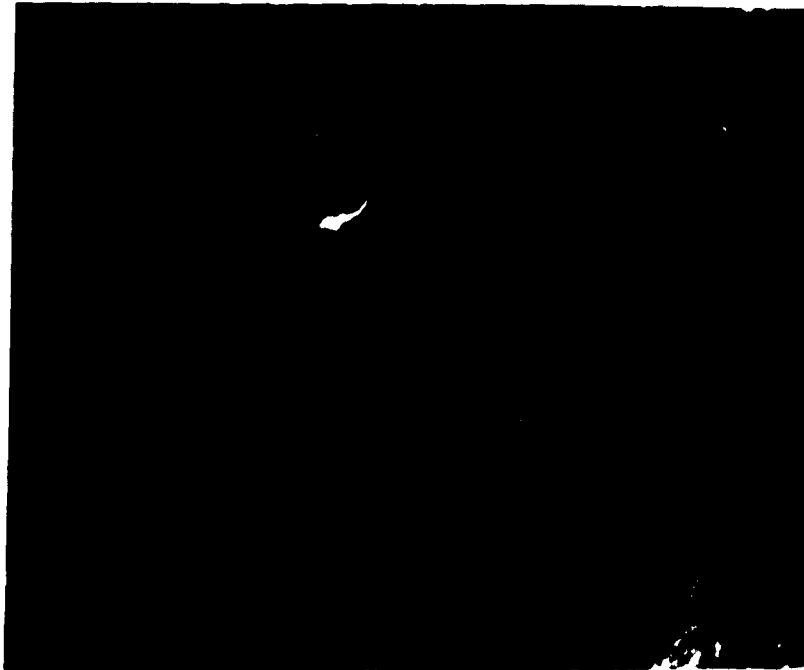


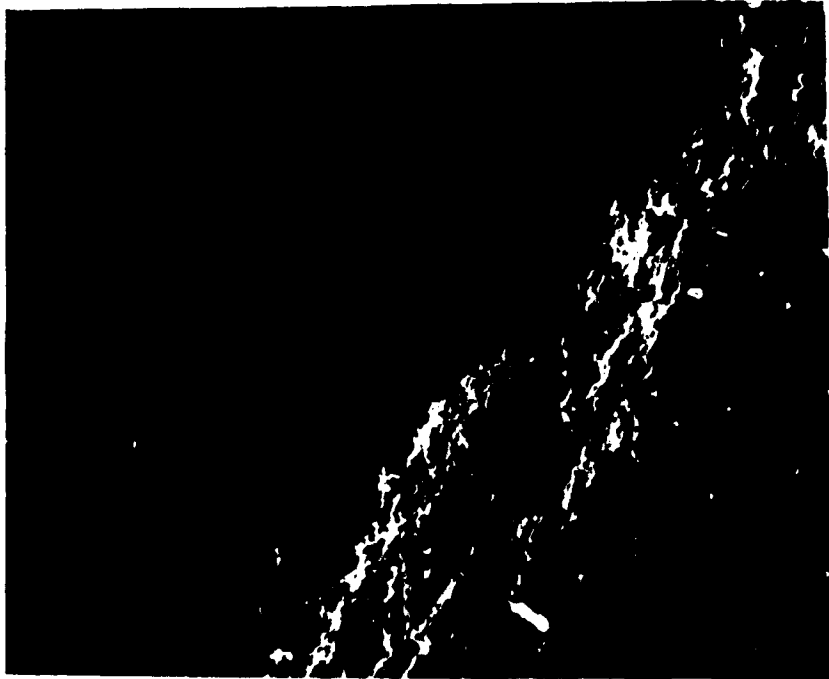
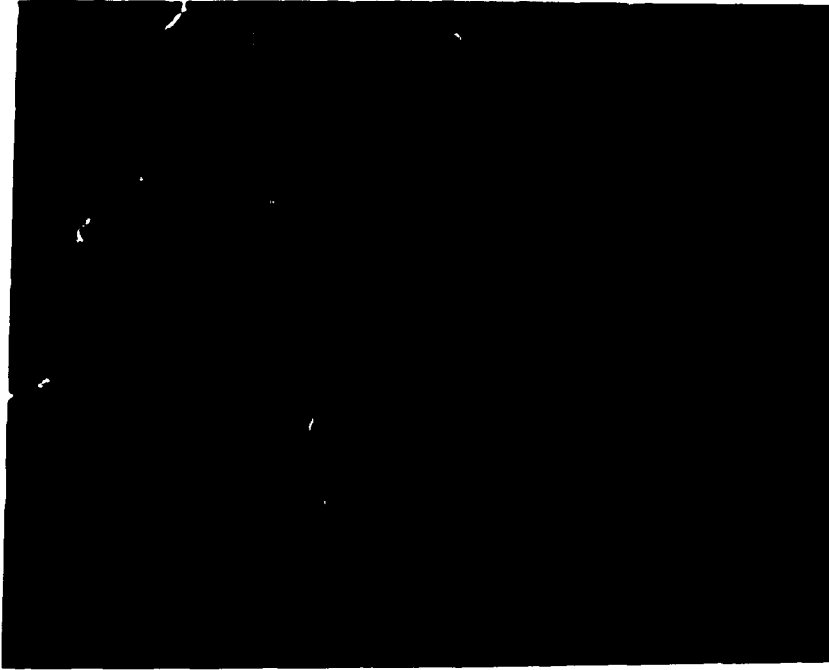
Figure 30. Interface of a pore and the fracture surface in a 40% porous fluorapatite-spinel ceramic fired at 1485 C (10,000X)

Figure 31. The fracture surface after the bend test of a 40% porous fluorapatite-spinel ceramic fired at 1485 C (10,000X)



Figure 32. SEM picture of the 40% porous fluorapatite-spinel ceramic fired at 1485 C showing the grain structure inside a pore (10,000X)

Figure 33. Fracture surface after the bend test of a nonporous fluorapatite-spinel ceramic fired at 1485 C (300X)



intergranular type although some flat surfaces that look like cleavage planes in a transgranular fracture are visible in the photographs. Figure 32 shows a pore region of the same ceramic. The grain structure is quite different than the structure in Fig. 22 although the compositions are the same. However, the ceramic in Fig. 22 was fired at 1600 C, but the ceramic in Fig. 28 through Fig. 32 was fired at 1485 C.

Figures 33 through 35 show the fracture surface of a nonporous fluorapatite-spinel ceramic at different magnifications. The ceramic was fired at 1485 C and it was fractured in the three-point bend test. The fracture type again appears to be intergranular.

Solubility Studies

The results of the weight changes of the bars exposed to Ringer's solution are summarized in Table 7. $\overline{\Delta W}_b$ is the mean difference in weight after removal from Ringer's solution but before ultrasonic cleaning. $\overline{\Delta W}$ is the mean difference in weight after ultrasonic cleaning. Table 7 indicates that most of the bars have gained some weight after exposure to Ringer's solution. After ultrasonic cleaning, the difference in weight became smaller, but there was still a net weight increase when compared with the weight before exposure.

Figure 34. Fracture surface of the nonporous fluorapatite-spinel ceramic fired at 1485 C (3000X)

Figure 35. Fracture surface of the nonporous fluorapatite-spinel ceramic fired at 1485 C (10,000X)

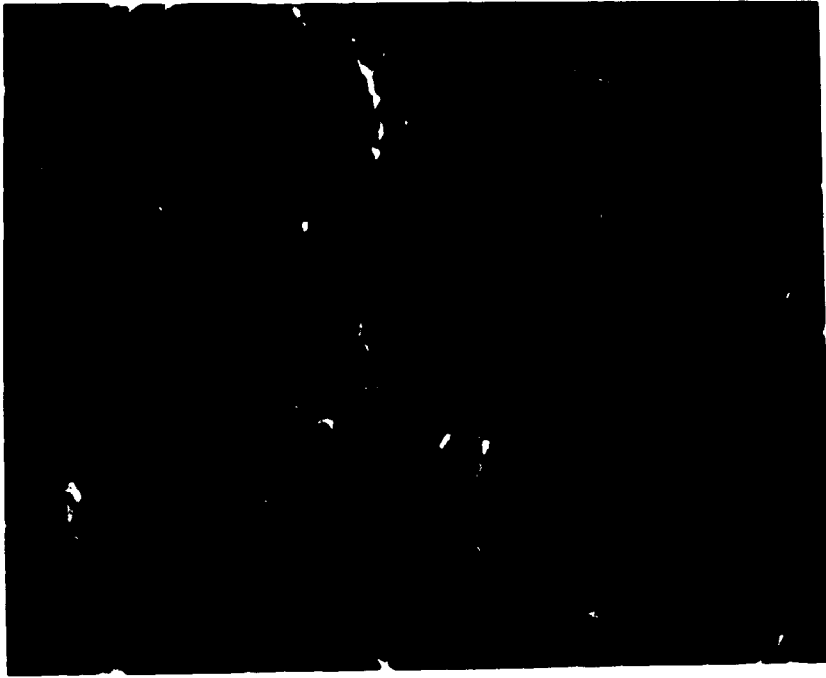


Table 7. Weight changes of the bars exposed to Ringer's solution

POROSITY (%)	EXPOSURE (months)	$\overline{\Delta W}_b$ (%)	$\overline{\Delta W}$ (%)
0	10	0.34	0.26
0	8	0.05	0.01
0	6	0.02	-0.01
0	5	0.06	-0.01
0	4	0.01	-0.01
30	10	0.77	0.61
40	10	2.45	2.14
40	8	2.19	1.98
40	6	1.03	1.15
40	5	1.21	0.84
40	4	1.27	1.31
50	8	3.24	2.93
50	6	1.53	1.65
50	5	2.08	1.51
50	4	2.07	1.85

The solutions in which the porous and nonporous bars stayed for 10 months were chemically analysed for dissolved F^- and Al^{3+} . The results are shown in Table 8.

Table 8. Amount of F^- and Al^{3+} dissolved in Ringer's solution due to the 10 months exposure of fluorapatite-spinel bars

	F^- (mg/l)	Al^{3+} (mg/l)
Solution of nonporous bars	1.0	1.0
Solution of 30% porous bars	31.0	9.0
Solution of 40% porous bars	0.2	580

Each group of bars was kept in 100 cc of Ringer's solution for 10 months. F^- and Al^{3+} were the only ions in the fluorapatite-spinel ceramic that were not also present in Ringer's solution. Therefore, the solutions were analyzed for only these two ions to test the solubility of the ceramic. The results indicate that the ceramic bars showed some solubility in Ringer's solution. The concentration of Al^{3+} in the solution of 40% porous bars is unreasonably high; therefore, contamination of the

solution during the analysis is suspected.

The distilled water, used for the ultrasonic cleaning of the bars that stayed in Ringer's solution for 10 months, was also analyzed for F^- and Al^{3+} that may come from the ceramic, and for Na^+ , K^+ , SO_4^{2-} , inorganic carbon and Cl^- , which can only come from the Ringer's solution. The ultrasonic cleaning water was also analyzed for PO_4^{3-} , Ca^{2+} and Mg^{2+} , the ions that were present both in the ceramic and in Ringer's solution. The results are shown in Table 9.

Table 9. Analysis of the ultrasonic cleaning water for the ions present in the ceramic and in Ringer's solution

Ions	mg/l
F^-	2.0
Al^{3+}	9.8
Na^+	66.0
K^+	5.39
SO_4^{2-}	3.67
IC	11.0
Cl^-	87.0
PO_4^{3-}	0.11
Ca^{2+}	8.16
Mg^{2+}	0.39

It can be seen from Table 9 that the salts of the Ringer's solution were deposited on the ceramics during their exposure and part of these salts were removed during ultrasonic cleaning. Presence of F^- and Al^{3+} in the cleaning solution suggest that some of the F^- and Al^{3+} , dissolved during exposure to the solution, were deposited on the surface of the ceramics during drying, and they were removed during ultrasonic cleaning.

The purpose of solubility tests in Ringer's solution was to determine if the fluorapatite-spinel ceramic would be soluble in a solution that is similar to tissue fluids. The weight change determinations of the ceramic after exposure to Ringer's solution, and the chemical analysis of Ringer's solution to check the presence of ions which can only come from the ceramic indicate that the fluorapatite-spinel ceramic will have some solubility in tissue fluids.

Soft Tissue Reaction Test

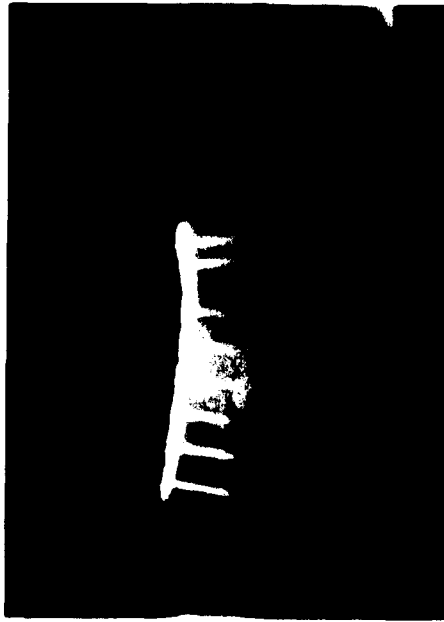
The four small bars of fluorapatite-spinel ceramic subcutaneously implanted in a dog were removed after 7.5 months for examination. No fibrous capsule or adhering tissues were present on the bars. Their surfaces showed no chemical attack by the tissue fluids in macroscopic examination.

Figure 36. Radiograph of the first implant right after the surgery

Figure 37. Radiograph of the first implant 8 weeks after the surgery. Note the small crack on one side and the gap between the bone and the implant. The side opposite to the crack shows bone growth next to the implant

Figure 38. Radiograph of the first implant 12 weeks after the surgery. The cracks on one side have become larger; however, the gap between the implant and the bone has become smaller due to new bone formation

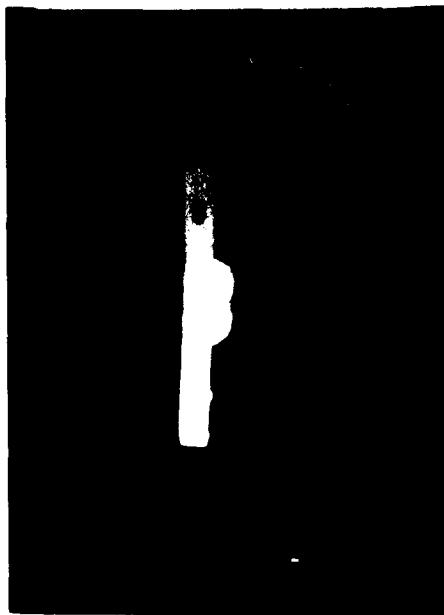
Figure 39. Radiograph of the first implant 16 weeks after the surgery showing the cracked ceramic on one side and dense bone formation on the opposite side



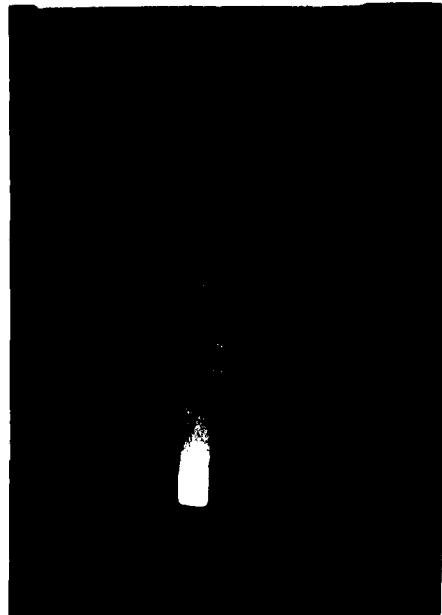
36



37



38



39

Implants In-Vivo

Radiographic examination of the first bone bridge revealed the presence of a crack in the ceramic 2 months after implantation (Fig. 37). During the removal of the implant 11 months after implantation, it was noticed that the crack had probably started from one of the two transverse screw holes in the ceramic and had progressed all the way through the cross section of the ceramic. Radiographic examination revealed that one screw was becoming loose, and there was some relative motion between the ceramic and the bone on one side, while the other side seemed to be firmly fixed (Fig. 40). There was denser bone formation on the side that was fixed firmly.

The second bone bridge turned out to be too big in diameter compared to the femur it was implanted in. However, this did not cause any problems related to bone ingrowth into the ceramic (Fig. 42 - Fig. 44). It was seen that the implant was firmly fixed (Fig. 43), and dense bone formation had occurred around the sides at both ends by 36 weeks. The steel bone plate used for the attachment of the implant to the bone was removed after 65 weeks (Fig. 45). The implant was left in place to follow up its performance without the bone plate. Six weeks after the removal of the bone plate, it was seen that the ceramic had fractured through one of the

Figure 40. Radiograph of the first implant 16 weeks after the surgery showing one of the screws becoming loose

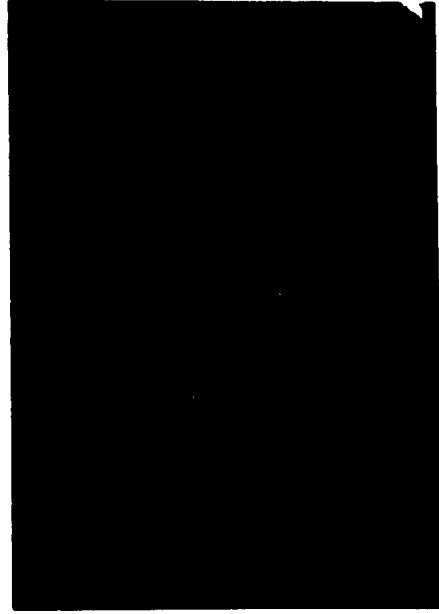
Figure 41. Radiograph of the first implant 40 weeks after the surgery showing the loose screw and the nut.

Figure 42. Radiograph of the second implant right after the surgery. Note difference in diameters of the implant and the bone

Figure 43. Radiograph of the second implant 36 weeks after the surgery showing dense bone formation around the implant



40



41



42

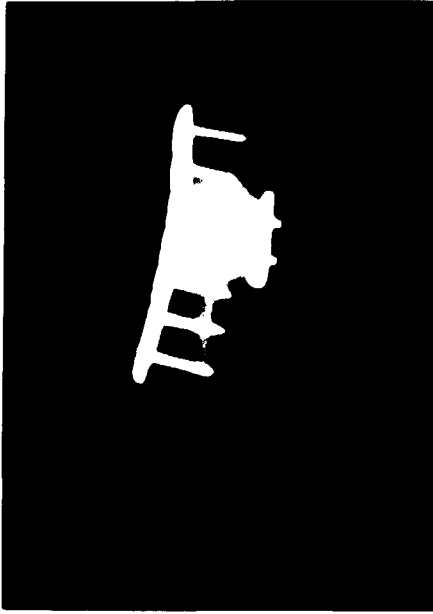


43

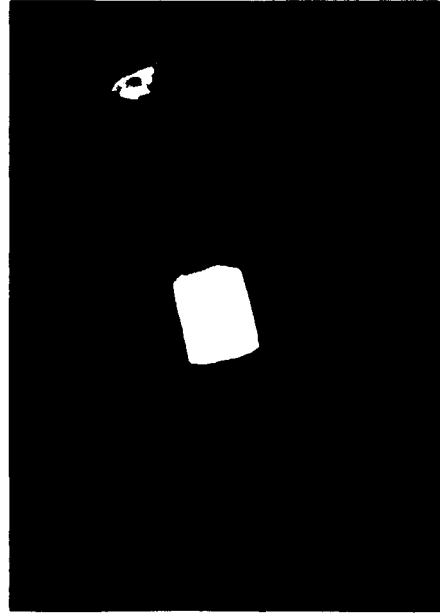
Figure 44. Radiograph of the second implant 65 weeks after the surgery

Figure 45. Radiograph of the second implant after the removal of the bone plate, 65 weeks after the implantation

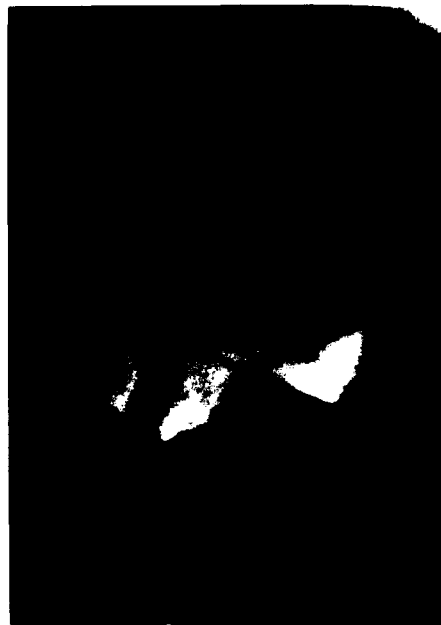
Figure 46. Radiograph of the second implant 5 weeks after the removal of the bone plate showing the fracture through one of the screw holes although the bone-implant interface at both ends is undamaged



44



45



46

transverse screw holes. However, both ends of the ceramic were firmly fixed to the bone (Fig. 46).

Microscopic Analysis of the Implant-Tissue Sections

Thin sections of the first implant with the infiltrated tissue (Fig. 47) were studied under polarized transmitted light using a gips plate in the Ultraphot II light microscope. This study revealed that the pores of the ceramic were completely infiltrated by bone and no fibrous tissue was visible at the interface of bone and ceramic at a 100X magnification (Fig. 48 -Fig. 53). However, thick collagenous fibrous tissue was visible around the holes for the metal screws. Some motion between the ceramic and the stainless steel screws was expected since the screw holes in the ceramic were not threaded, which caused the formation of the fibrous tissue around the screws (Fig. 54 -Fig. 58).

The axial hole of the implant was completely filled with cancellous bone as can be seen from Fig. 59. It is believed that it is very advantageous to have an axial hole in the implant for the complete infiltration of pores by bone.

No adverse tissue reactions or inflammation were observed in the soft tissues in contact with the implant.

Figure 47. Polished thin section of the first implant showing the bone at one end and the fracture surface on the other.

One of the screw holes passing through the ceramic is also visible in the picture

Figure 48. Micrograph of the bone-implant interface at 25X. The dark area is the ceramic.

The regions of spongy and cortical bone are also visible due to the polarized transmitted light used during the microscopic examination

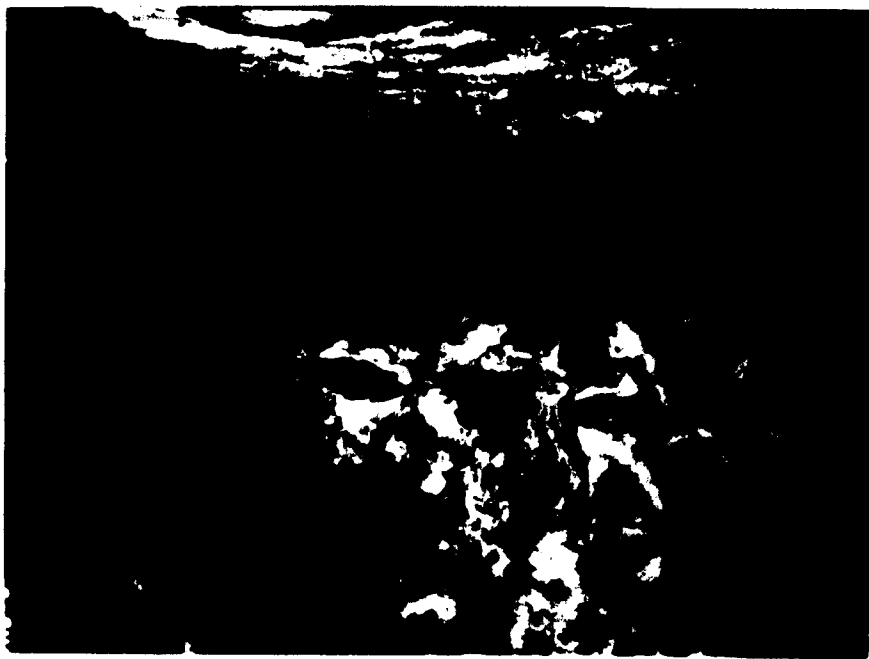
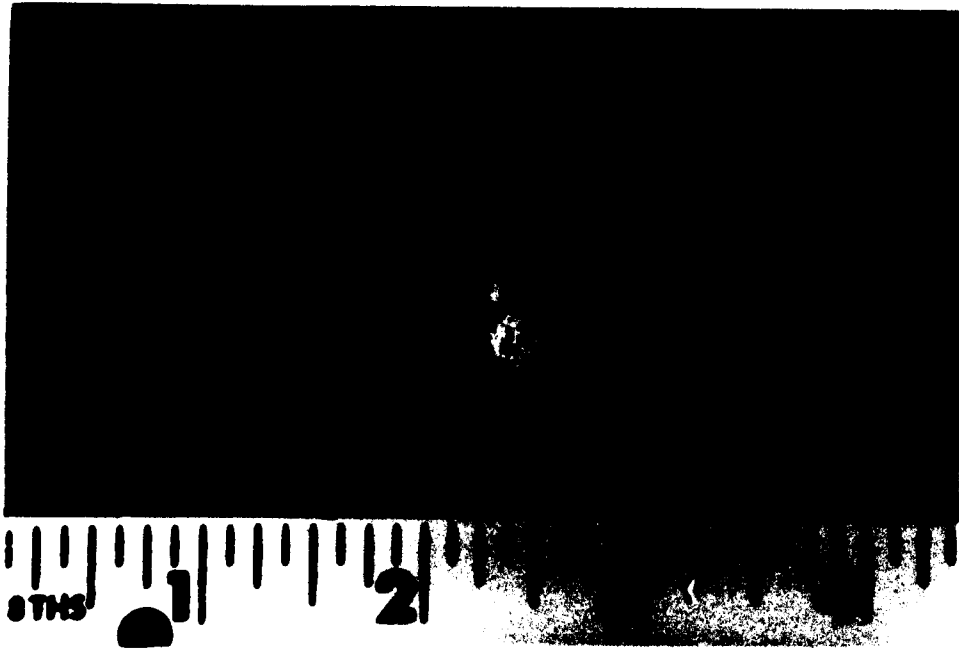


Figure 49. Micrograph of the bone-implant interface at 25X showing the Haversian system in the bone, and infiltration of the pores of the ceramic by bone (Polarized transmitted light)

Figure 50. Micrograph of the bone-implant interface at 25X showing complete infiltration of the pores in the ceramic by bone. Soft tissue adjacent to the cortical bone is also visible (Polarized transmitted light)



Figure 51. Micrograph of the bone-implant interface at 100X showing direct bonding of the bone to the implant and no fibrous capsule at the interface (Polarized transmitted light)

Figure 52. Micrograph of the bone-implant interface at 100X showing infiltration of pores by bone without a fibrous capsule. The Haversian system in the bone is clearly visible (Polarized transmitted light)

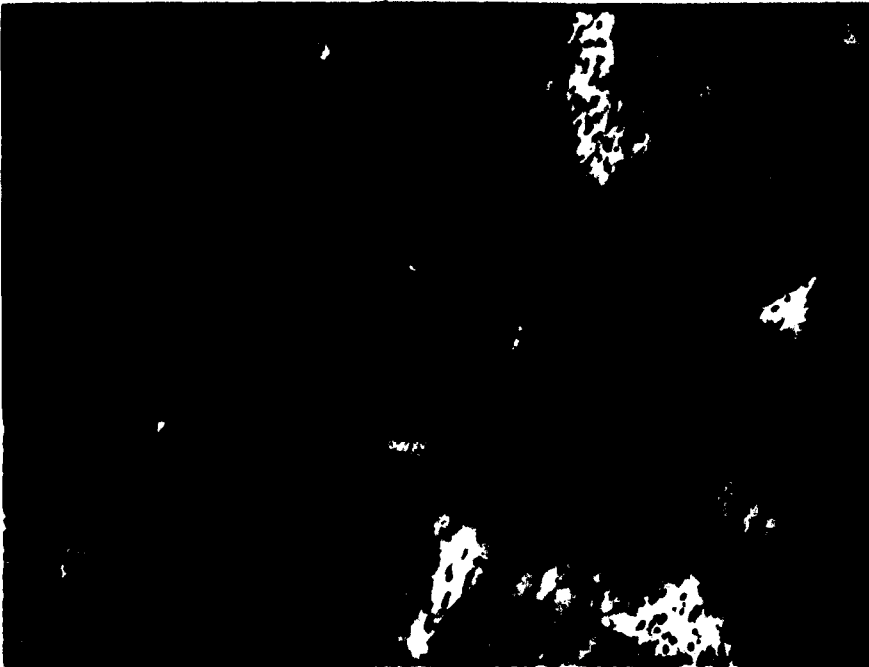
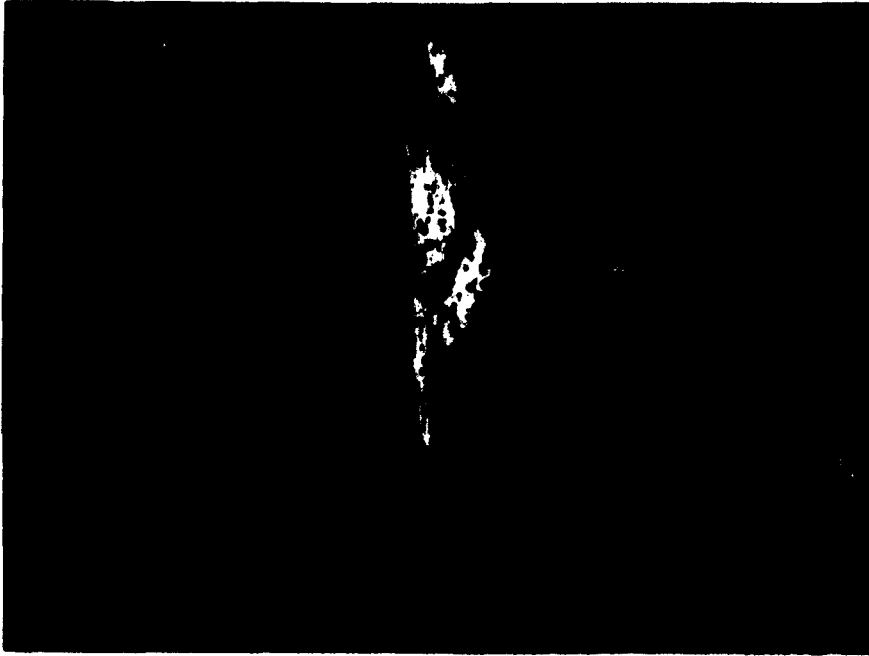


Figure 53. Micrograph of the implant at the fractured end showing the separated crystals and bone formation among them (25X, polarized transmitted light)

Figure 54. Micrograph of the implant around the transverse screw hole (25X, polarized, transmitted light)



Figure 55. Micrograph of the implant around the screw hole showing the fibrous tissue around the hole, and bone in between the fibrous tissue and the ceramic (25X, polarized transmitted light)

Figure 56. Micrograph of the implant around the screw hole showing the fibrous tissue (100X, polarized transmitted light)

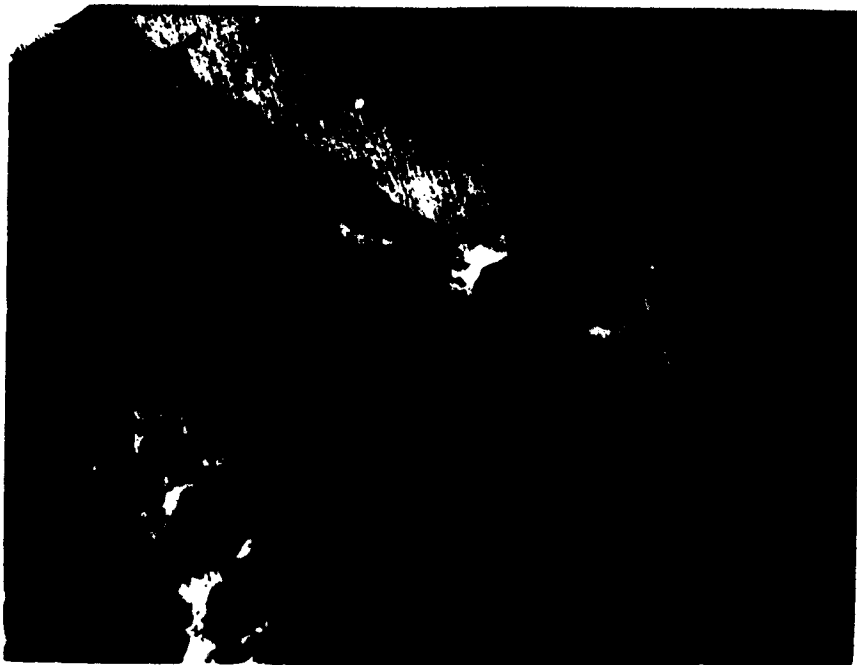
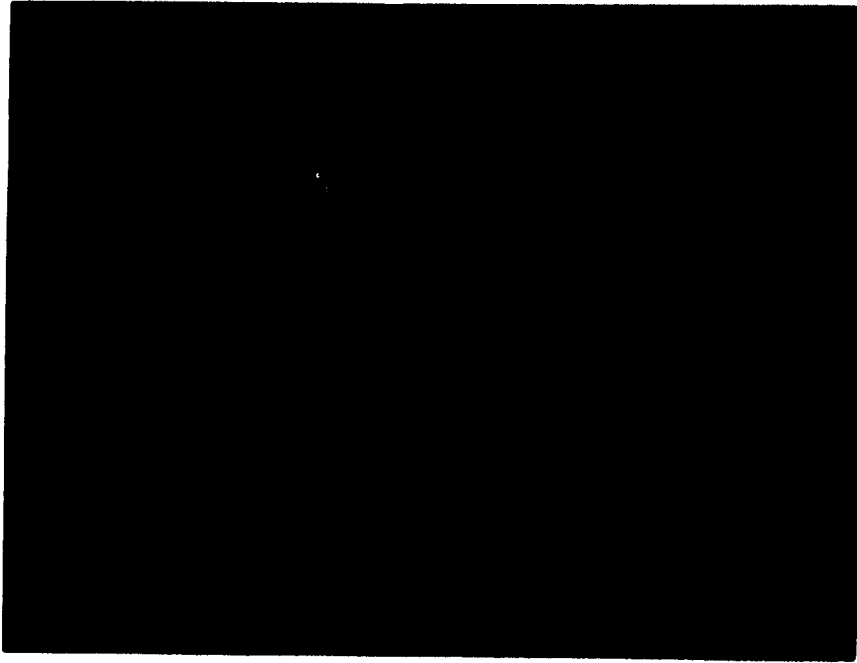


Figure 57. Micrograph showing the fibrous tissue around the screw hole, and bone between the ceramic and fibrous tissue (100X, polarized transmitted light)

Figure 58. Longitudinal section through the screw hole showing the thread marks with fibrous tissue and bone around them (25X, polarized transmitted light)



Figure 59. Micrograph of the longitudinal section of the axial hole in the ceramic showing the infiltration of spongy bone (43X, polarized transmitted light)



CONCLUSION

The fluorapatite-spinel ceramic with interconnected pores was found to be a suitable material as a permanent hard tissue implant. In-vivo tests proved it to be inert and non-inflammatory. Absence of a fibrous capsule at the bone-implant interface showed that the foreign body response mechanism will not be seen for this type of implant. Complete infiltration of pores by bone makes the fluorapatite-spinel ceramic a suitable alternative to permanent bone grafts.

Although the first implant cracked in situ, and the second implant fractured after the removal of the bone plate, it can be predicted that the mechanical properties can be considerably improved by using higher firing temperatures and keeping the amount of porosity about 30%. Avoiding grog in the powder will also help to improve the strength. Both of the implants were fired at 1450 C; however, the results of the bend test showed that higher strengths can be achieved by firing at 1485 C. Therefore, it is possible to produce implants with better mechanical properties.

Removal of the bone plate is not usually required; therefore, better performance of the implant under loads can be ensured by keeping the bone plate permanently.

BIBLIOGRAPHY

1. Predecki, P.; Stephan, J. E.; Auslander, B. A.; Mooney, V. L.; Kirkland, K. J. J. Biomed. Mater. Res. 1972, 6, 375-400.
2. Sauer, B. W.; Weinstein, A. M.; Klawitter, J. J.; Hulbert, S. F.; Leonard, R. L.; Bagwell, J. G. J. Biomed. Mater. Res. 1974, 5, 143-153.
3. Schneider, P.; Lutz, F.; Muhlemann, H. R. J. Oral Implantol. 1979, 8, 371-379.
4. Ferraro, J. W. Plast. Reconstr. Surg. 1979, 63(5) 634.
5. Hulbert, S. F., presented at the National Conference on Use of Ceramics in Surgical Implants, Clemson University, Clemson, S.C., Jan 1969.
6. Heimke, G.; Griss, P.; Jentschura, G.; Werner, E. J. Biomed. Mater. Res. 1979, 13(1), 57-65.
7. Salzer, M.; Knahr, K.; Locke, H.; Stark, N. Clin. Orthop. Jul-Aug 1978, 134, 80-86.
8. Griss, P.; Krempien, B.; Von Andrian-Werburg, H.; Heimke, G.; Fleiner, R.; Diehm, T. J. Biomed. Mater. Res. 1974, 5, 39-48.
9. Semlitsch, M.; Lehman, M.; Weber, H.; Doerre, E.; Willert, H. G. J. Biomed. Mater. Res. 1977, 11, 537-552.
10. Hastings, G. W. Biomat., Med. Dev., Art. Org. 1979, 7(1), 1-22.
11. Pedersen, K. N.; Haanaes, H. R. Acta Odontol. Scand. 1979, 37(4), 181-187.

12. Pedersen, K. N.; Haanaes, H. R. Acta Odontol. Scand. 1979, 37(6), 347-352.
13. Hench, L. L.; Paschall, H. A. J. Biomed. Mater. Res. 1973, 4, 25-42.
14. Ogino, M.; Ohuchi, F.; Hench, L. L. J. Biomed. Mater. Res. 1980, 14, 55-64.
15. De Groot, K. Biomaterials 1980, 1, 47-50.
16. Jarcho, M.; Kay, J. F.; Gumaer, K. I.; Doremus, R. H.; Drobeck, H. P. J. Bioeng. 1977, 1, 79-92.
17. Levin, M. P.; Getter, L.; Adrian, J.; Cutright, D. E. J. Clin. Periodontol. 1974, 1, 197-205.
18. Levin, M. P.; Getter, L.; Cutright, D. E.; Bhaskar, S. N. Oral Surg. 1974, 38, 344-351.
19. Levin, M. P.; Getter, L.; Cutright, D. E.; Bhaskar, S. N. J. Biomed. Mater. Res. 1975, 9, 183-195.
20. Nery, E. B.; Lynch, K. L.; Hirthe, W. M.; Mueller, K. H. J. Periodontol. 1975, 46, 328-347.
21. Peelen, J. G. J.; Rejda, B. V.; De Groot, K. J. Bioeng. 1977, 1, 93-97.
22. Cameron, H. U.; Macnab, I.; Pilliar, R. M. J. Biomed. Mater. Res. 1977, 11, 179-186.
23. Jarcho, M.; Salsbury, R. L.; Thomas, M. B.; Doremus, R. H. J. Mater. Sci. 1979, 14, 142-150.
24. Janikowski, T.; McGee, T. D. Proc. Iowa Acad. Sci. 1970, 76, 113-118.
25. McGee, T. D.; Wood, J. L. J. Biomed. Mater. Res. Symposium 1974, 5, 137-144.

26. Howden, G. F. In "Mechanical Properties of Biomaterials"; Hastings, G. W.; Williams, D. F., Eds.; John Wiley & Sons Ltd.: New York, 1980; Chapter 36.
27. Koster, K.; Ehard, H.; Kubicek, J.; Heide, H. Z. Orthop. 1979, 118, 398-403.
28. Park, J. B. "Biomaterials - An Introduction"; Plenum Press: New York, 1979; Chapter 7.
29. "Encyclopaedia Britannica"; Encyclopaedia Britannica, Inc.: Chicago, Ill., 1973; Vol. 21, p. 757.
30. Holmes, R. E. Plast. Reconstr. Surg. 1979, 63(5), 626-633.
31. Ferraro, J. W. Plast. Reconstr. Surg. 1979, 63(5), 640.
32. Duff, E. J.; Grant, A. A. In "Mechanical Properties of Biomaterials"; Hastings, G. W.; Williams, D. F., Eds.; John Wiley & Sons LTD.: New York, 1980; Chapter 38.
33. McCann, H. G. Arch. Oral Biol. 1968, 13, 987-1001.
34. Davis, S. D.; Gibbons, D. F.; Martin, R. L.; Levitt, S. R.; Smith, J.; Harrington, R. V. J. Biomed. Mater. Res. 1972, 6, 425-449.
35. Levin, E. M.; Robbins, C. R.; McMurdie, H. F. "Phase Diagrams for Ceramists"; American Ceramic Society: Columbus, Ohio, 1964; p. 106.
36. "Handbook of Chemistry and Physics", 60th ed.; Weast, R. C., Ed.; CRC Press, Inc.: Boca Raton, Florida, 1980; p. B-93.
37. Hopkins, R. H.; Damon, D. H.; Piotrowski, P.; Walker, M. S.; Uphoff, J. H. J. Appl. Phys. 1971, 42(1),

272-275.

38. Richardson, W. C., Jr.; Klawitter, J. J.; Sauer, B. W.; Pruitt, J. R.; Hulbert, S. F. J. Biomed. Mater. Res. Symposium 1975, 6, 73-80.
39. Karagianes, M. T.; Westerman, R. E.; Rasmussen, J. J.; Marshall, R. P. J. Biomed. Mater. Res. Symposium 1974, 5(2), 391-399.
40. "X-Ray Powder Data File"; Smith, J. V., Ed.; ASTM: Philadelphia, Pa., 1967; 5-0672.
41. "Powder Diffraction File (Inorganic)"; Berry, L. G., Ed.; Joint Committee on Powder Diffraction Standards: Philadelphia, Pa., 1972; 15-876.
42. Grenoble, D. E.; Katz, J. L.; Dunn, K. L.; Gilmore, R. S.; Murty, K. L. J. Biomed. Mater. Res. 1972, 6, 221-233.
43. Kingery, W. D.; Bowen, H. K.; Uhlmann, D. R. "Introduction to Ceramics", 2nd ed.; John Wiley & Sons, Inc.: New York, 1976; Chapter 15.
44. Lynch, J. F.; Ruderer, C. G.; Duckworth, W. H. "Engineering Properties of Selected Ceramic Materials"; American Ceramic Society: Columbus, Ohio, 1966; Chapter 5.
45. Anand, S. C.; St. John, K. R.; Moyle, D. D.; Williams, D. F. Ann. Biomed. Eng. 1977, 5, 410-420.
46. Katz, J. L. J. Biomech. 1971, 4, 455-473.
47. Evans, F. G. "Mechanical Properties of Bone"; Thomas: Springfield, Ill., 1973; p. 176.
48. Griffith, A. A. Philos. Trans. R. Soc. 1920, A221, 163.

49. Inglis, C. E. Trans. Inst. Nav. Arch. 1913, 55, 219.
50. Orowan, E. Z. Krist. 1934, A89, 327.
51. Orowan, E. Rep. Prog. Phys. 1948, 12, 185.
52. Irwin, G. R.; Kies, J. A. Welding J. 1952, 31, 450.
53. Dugdale, D. S. J. Mech. Phys. Solids 1960, 8, 100.
54. Weibull, W. Ing. Vetensk. Akad. 1939, Proc. 151, No. 153.
55. Clarke, F. J. P. Acta Met. 1964, 12, 139.
56. Gell, M.; Smith, E. Acta Met. 1967, 15, 253.
57. Charles, R. J. J. Appl. Phys. 1958, 29, 1549.
58. Wiederhorn, S. M. J. Am. Ceram. Soc. 1967, 50, 407.
59. Ryshkewitch, E. J. Am. Ceram. Soc. 1953, 36, 65.
60. "Inorganic Index to the Powder Diffraction File"; Smith, J. V., Ed.; American Society for Testing and Materials: Philadelphia, Pa., 1968.
61. "Powder Diffraction File (Inorganic)"; Smith, J. V., Ed.; ASTM: Philadelphia, Pa., 1967; 9-170.
62. Williams, R. J.; Lansford, E. M., Jr. "The Encyclopedia of Biochemistry"; Reinhold Publishing Corporation: New York, 1967; p. 594.
63. Snedecor, G. W.; Cochran, W. G. "Statistical Methods", 7th ed.; The Iowa State University Press: Ames, Iowa, 1980; Chapter 4.
64. "Chemical Engineers' Handbook", 5th ed.; Perry, R. H.; Chilton, C. H., Eds.; McGraw-Hill: New York, 1973; p. I-40.

ACKNOWLEDGMENTS

I would like to thank my major professor, Dr. T. D. McGee, for his guidance, invaluable suggestions and encouragement in this study, and also, throughout my education at the Iowa State University.

I also wish to express my appreciation to Dr. W. D. Hoefle for performing the implant surgeries, which the success of this study largely depended on.

Special thanks are due to all the other members of my committee for their invaluable suggestions.

Finally, I would like to thank my parents, Fatma and Haluk Aksaci, for their support and patience throughout the years.

APPENDIX A

Ringer's Solution

Ringer's solution is a salt solution which is approximately isotonic to the blood and to the lymph of mammals. Originally, it consisted of sodium chloride, potassium chloride, calcium chloride, and sodium bicarbonate. Various modifications of this solution are now in use. The composition of the solution used in this study was as follows (62):

	<u>mg/l</u>
NaCl	6800
KCl	400
CaCl	200
MgSO ₄	100
NaH ₂ SO ₄	125
NaHCO ₃	2200

APPENDIX B

Confidence Intervals for Means and the
Student's t Test

Student's t test enables us to compute confidence limits for the population mean, μ , of a random sample of size n from a normal distribution with an unknown population variance σ^2 . It is appropriate to use the t test when the sample size is small. The confidence limits for μ are calculated by using the following equation (63):

$$t = \frac{\bar{X} - \mu}{S/\sqrt{n}} \quad \text{Eq. 35}$$

where \bar{X} is the sample mean and S is the sample standard deviation, and t is the deviation of the estimate mean from the population mean. S is calculated from the equation:

$$S = \sqrt{\sum_{i=1}^n (X_i - \bar{X})^2 / (n - 1)} \quad \text{Eq. 36}$$

where X_i is the i^{th} observation in the sample.

When t is calculated from a single random sample of size n , the degrees of freedom are $(n-1)$. A table of

the t-distribution gives, for each probability at the top of a column, the value of t, (say t^*), such that $P[|t| > t^*]$ has the stated probability for the number of degrees of freedom in the row. $t_{0.05}$ gives the value of t when the probability of a larger value is 5%. If the calculated value for t is less than or equal to t^* ($|t| \leq t^*$) for the given number of degrees of freedom, and the selected probability, then the hypothesis $\bar{X} = \mu$ cannot be rejected. If $|t| \geq t^*$, the hypothesis $\bar{X} = \mu$ is rejected, which means that there is a statistically significant difference between the sample mean and the population mean.

APPENDIX C

Comparison of Means by the
Student's t Test

The hypothesis for this test is that the two population means μ_1 and μ_2 are equal. It is also assumed that the standard deviations of the two populations are equal (i.e., $\sigma_1 = \sigma_2$). The value of t is then calculated as follows (64):

$$t = \frac{\bar{X}_2 - \bar{X}_1}{S\sqrt{(1/n_1) + (1/n_2)}} \quad \text{Eq. 37}$$

where \bar{X}_1 and \bar{X}_2 are sample means, and $(S)^2$ is the pooled variance estimate of $\sigma^2 = \sigma_1^2 = \sigma_2^2$. $(S)^2$ is given by

$$(S)^2 = \frac{(n_1 - 1)S_1^2 + (n_2 - 1)S_2^2}{n_1 + n_2 - 2} \quad \text{Eq. 38}$$

where S_1 and S_2 are sample standard deviations.

The theoretical value of t can be found in the distribution table of t (64), corresponding to the selected probability level, and $(n_1 + n_2 - 2)$ degrees of freedom. If the calculated t is greater than this value, the hypothesis is refuted, and it is assumed that $\mu_1 \neq \mu_2$.